Small-Signal Stability Analysis and Current Control Reference Optimization Algorithm of DFIG-Based WT During Asymmetric Grid Faults

Xin Fang, Jun Yao, *Member, IEEE*, Ruikuo Liu, Yang Zhao, Peng Sun, and Sen Huang

***Abstract*—The stability issues of weak grid-connected doubly fed induction generator (DFIG) based wind turbines during asymmetric grid faults become very acute. In this article, a small-signal state-space model was established to deal with the stability problems of the DFIG system during asymmetric grid faults. Based on the model, the interaction mechanism between the power grid and the DFIG system during asymmetric faults is described and the modal analysis is performed. The analysis results show that the dominant unstable poles of the system are mainly affected by the phase-locked loop (PLL). Then, according to the vector relationships of voltages and currents, the effect of positive-sequence (PS) and negative-sequence (NS) *d*-axis currents on the PLL output angle is analyzed. It is pointed out that the system stability can be effectively improved by injecting reasonable *d*-axis components of PS and NS currents into the power grid during faults. Furthermore, considering the current capacity limitation of DFIG, a novel PS and NS current control reference optimization algorithm is proposed, which can suppress the oscillation of the system. Finally, the correctness of the theoretical analysis and the effectiveness of the proposed control strategy are validated by the simulation and experiments.**

***Index Terms*—Asymmetric grid faults, doubly fed induction generator (DFIG), optimal current control reference algorithm, phase-locked loop (PLL), small-signal stability.**

Nomenclature

$\boldsymbol{U}, \boldsymbol{I}, \Psi$	Voltage, current, and flux linkage vectors.
ω_{1+} and ω_r	Synchronous and rotor angular frequency.
R_s and R_r	Stator and rotor resistances of DFIG.
L_s, L_r, and L_m	Stator, rotor, and mutual inductances of DFIG.
R_g and L_g	Resistance and inductance of the grid-side reactor.
$\theta_{\mathrm{pll}+}$ and $\omega_{\mathrm{pll}+}$	Output angle and angular frequency of PLL.
C_f	Filter capacitor.
C	DC-link capacitor.
σ	Coefficient of magnetic dispersion.
p	Differential operator.
Subscripts	
d and q	dq-axis components in the PLL reference frame.
s, r, g, and *f*	Stator-, rotor-, grid-side, and fault-point quantities.
0	Initial value.
$+$ and $-$	Positive- and negative-sequence components.
b	Base value.
Superscripts	
$+$ and $-$	Positive and negative synchronous reference frames.
c	Conjugate component.

Manuscript received August 8, 2020; revised October 16, 2020 and November 21, 2020; accepted November 26, 2020. Date of publication December 9, 2020; date of current version March 5, 2021. This work was supported in part by the Joint Research Fund in Smart Grid (U1966208) under cooperative agreement between the National Natural Science Foundation of China and State Grid Corporation of China, in part by the National Natural Science Foundation of China under Grant 51977019, in part by the 111 Project of China under Grant B18062, and in part by the State Grid Chongqing Electric Power Company under Grant 52202319004G. Recommended for publication by Associate Editor M. S. ElMoursi. *(Corresponding author: Jun Yao.)*

Xin Fang, Jun Yao, Yang Zhao, Peng Sun, and Sen Huang are with the State Key Laboratory of Power Transmission Equipment and System Security and New Technology, School of Electrical Engineering, Chongqing University, Chongqing 400044, China (e-mail: fangxin1014@163.com; jyao@cqu.edu.cn; zhao_yang@cqu.edu.cn; sp1718120621@163.com; huangsenwarm@163.com).

Ruikuo Liu is with the Institute of Science and Technology, China Three Gorges Corporation, Beijing 100038, China (e-mail: liuruikuo1986@163.com).

Color versions of one or more of the figures in this article are available at https://doi.org/10.1109/TPEL.2020.3042514.

Digital Object Identifier 10.1109/TPEL.2020.3042514

I. Introduction

In recent years, the wind power technology has developed rapidly [1]. The wind power generation equipment has been widely installed worldwide [2]. Since wind farms are often located in remote areas, the long-distance transmission and the high line impedance have become the critical factors for wind farms to connect to the grid [3], [4]. Consequently, the short-circuit ratio (SCR) of the system is lower and grid faults occur frequently, especially asymmetric faults [5], [6]. In addition, the stator of the doubly fed induction generator (DFIG) based wind turbine (WT) is directly coupled to the grid and it is very sensitive to the grid faults [7]. The dips of the voltage in the weak grid will bring undesirable dynamics to the DFIG system and may cause the small-signal instability of the system [8]. Therefore, the small-signal stability of the DFIG system during asymmetric grid faults needs to be investigated.

Some pieces of literature have studied the dynamic stability of the DFIG system during grid faults. Shin *et al*. [9] analyzed the relationship between the phase-locked loop (PLL) and the stability of the DFIG system, and proposed an improved PLL structure to improve the low-voltage ride-through (LVRT) capability of the system. Ye *et al*. [10] studied the influence of rotor

dynamic on the small-signal behavior of the DFIG system. In [11], the influence of various factors on the dynamic stability of the DFIG system under grid faults is analyzed in detail by adopting the state-space model. These pieces of literature mainly investigated the stability issue of the DFIG system under the symmetric grid fault. However, the stability issue of the DFIG system during the symmetric fault is completely different from that during the asymmetric faults, which is more complicated. When the asymmetric fault occurs, the voltages and currents contain both positive-sequence (PS) and negative-sequence (NS) components. In addition, due to the asymmetry of the transmission line structure, the sequence impedances of the system are no longer independent. As a result, there is a dynamic coupling between the PS voltage and the NS current, and the NS voltage and the PS current. What is more, the coupling of the sequence impedances makes the system exhibit the characteristic of multiple inputs and multiple outputs, which leads to the stability analysis method, and the instability mechanism of the DFIG system during the asymmetric faults is completely different from that during the symmetric fault. Considering that asymmetric faults occur more frequently in the power grid, it is necessary to study the stability issue of the system during the asymmetric faults.

Chen *et al*. [13]–[19] discussed the stability of the renewable energy system and the corresponding control strategy under asymmetric faults. In [12], the analyses of stability problems during faults fall into two categories: first, large-disturbance stability analysis, which focuses on whether or not the system can move from the original equilibrium to a new one during the transients; second, small-signal stability analysis, which evaluates whether or not the equilibrium of the system is a stable one. Chen *et al*. [13] and Alsmadi *et al*. [14] analyze the transient characteristics of DFIG under asymmetric faults and propose improved control schemes. However, whether it is in [13] or [14], the phenomenon investigated belongs to the large-disturbance stability analysis, and the small-signal stability problem of the DFIG system is not involved.

In terms of the current reference algorithm during asymmetric faults, Neumann *et al*. [15] and [16] discussed the influence of the PS and NS q-axis currents injection on the grid-connected converter system stability but the interaction mechanism between the converter system and the power grid is not explained. Moreover, unlike the grid-connected converter, the special structure of the DFIG system makes it exhibit multiport parallel characteristics. Therefore, it is more complicated to analyze the interaction law between the DFIG-based WT and the power grid during asymmetric faults and the stability problem is more serious. In [17], based on the mathematical model of the DFIG system, a control strategy is proposed, which uses the four control variables of the d-axis and q-axis components of PS and NS currents to achieve different control goals. However, it can only achieve a part of the control goals due to the limited control variables [18]. Moreover, it does not consider the coupling relationship between the PS and NS voltages and currents, which is caused by the interaction between the power grid and the DFIG system. In [19], based on the impedance method, a frequency-domain model is established for the analysis of the frequency coupling characteristics of the DFIG system under asymmetric faults. However, the small-signal stability and the corresponding improved control strategy are not researched.

As mentioned above, the small-signal stability problem of the DFIG system considering the interaction between the power grid and the DFIG system during asymmetric faults has not been fully investigated. To fill gaps in the existing literature, combining with the state-space method and space-vector synthesis method, a time-domain model of the grid-connected DFIG system considering the coupling relationship between PS and NS voltages and currents is established for the first time. Based on the model, the interaction mechanism between the power grid and the DFIG system during asymmetric faults is described in detail. On the basis of the previous analysis, the main contributions of this article can be summarized as follows.

1) According to the vector relationship of voltages and currents, it is pointed out that the stability of the system can be effectively improved by injecting reasonable PS and NS d-axis currents into the power grid during asymmetric faults and the optimal reference values of PS and NS currents are derived.
2) Considering the current capacity limitation of the DFIG-based WT, a novel PS and NS current control reference optimization algorithm is proposed, which can significantly increase the damping of the PLL and improve the small-signal stability of the system during asymmetric faults.

This article is organized as follows. The investigated DFIG system and its small-signal state-space model during asymmetric faults is established in Section II. In Section III, the small-signal stability of the DFIG system is analyzed and a novel optimal current control reference algorithm is proposed. Section IV presents the simulation and experimental results. Finally, Section V concludes the article.

II. Small-Signal State-Space Model of the DFIG System During Asymmetric Grid Faults

Fig. 1 shows a configuration diagram of the DFIG-based WT under asymmetric faults [20], [21], where an *RL*-type grid impedance is considered. The motor convention is selected as the positive direction of the current. The detailed asymmetrical fault ride through (FRT) control scheme of the DFIG system is provided in Fig. 1. It should be noted that this article focuses on the small-signal stability of the quasi-static stage during the asymmetric faults, in which the transient components are considered to have completely attenuated [22]. Therefore, the crowbar on the rotor side or the chopper on the dc side is deactivated during this stage. In order to study the small-signal stability characteristics of the DFIG system, its nonlinear mathematical model with high order was linearized at the stable operating point during faults in this section. In this article, the small-signal model is established in the PLL $dq^{\pm}$ frames, as shown in Fig. 2.

A. DFIG Model

According to the motor convention, the per-unit (p.u.) voltage and flux linkage equations of the DFIG during asymmetric faults

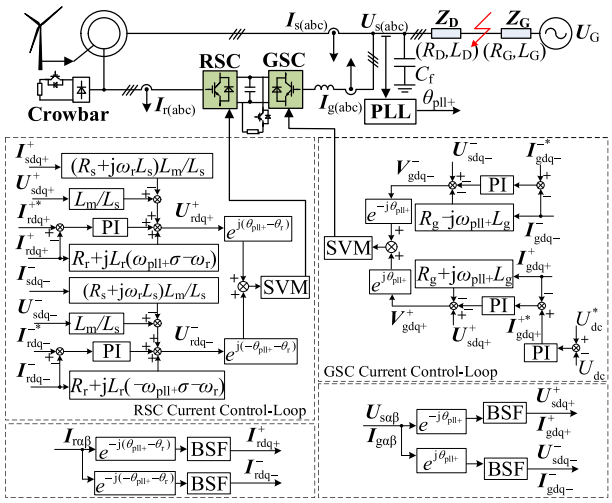

Fig. 1. Block diagram of the DFIG system during asymmetric grid faults.

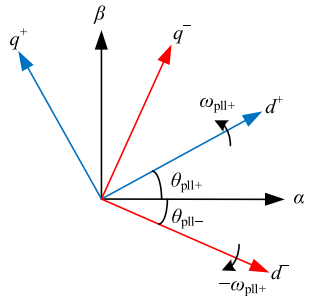

Fig. 2. Spatial position diagram of PLL $dq^{\pm}$ reference frames.

can be expressed as [23]

$$\begin{cases} \boldsymbol{U}^+_{sdq+} = R_s \boldsymbol{I}^+_{sdq+} + \dot{\boldsymbol{\psi}}^+_{sdq+} \big/ \omega_b + j\omega_{\text{pll}+} \boldsymbol{\psi}^+_{sdq+} \\ \boldsymbol{U}^-_{sdq-} = R_s \boldsymbol{I}^-_{sdq-} + \dot{\boldsymbol{\psi}}^-_{sdq-} \big/ \omega_b - j\omega_{\text{pll}+} \boldsymbol{\psi}^-_{sdq-} \\ \boldsymbol{U}^+_{rdq+} = R_r \boldsymbol{I}^+_{rdq+} + \dot{\boldsymbol{\psi}}^+_{rdq+} \big/ \omega_b + j(\omega_{\text{pll}+} - \omega_r) \boldsymbol{\psi}^+_{rdq+} \\ \boldsymbol{U}^-_{rdq-} = R_r \boldsymbol{I}^-_{rdq-} + \dot{\boldsymbol{\psi}}^+_{rdq+} \big/ \omega_b - j(\omega_{\text{pll}+} + \omega_r) \boldsymbol{\psi}^-_{rdq-} \end{cases} \tag{1}$$

$$\begin{cases} \boldsymbol{\psi}^+_{\text{sdq}+} = L_{\text{s}} \boldsymbol{I}^+_{\text{sdq}+} + L_{\text{m}} \boldsymbol{I}^+_{\text{rdq}+} \\ \boldsymbol{\psi}^-_{\text{sdq}-} = L_{\text{s}} \boldsymbol{I}^-_{\text{sdq}-} + L_{\text{m}} \boldsymbol{I}^-_{\text{rdq}-} \\ \boldsymbol{\psi}^+_{\text{rdq}+} = L_{\text{m}} \boldsymbol{I}^+_{\text{sdq}+} + L_{\text{r}} \boldsymbol{I}^+_{\text{rdq}+} \\ \boldsymbol{\psi}^-_{\text{rdq}-} = L_{\text{m}} \boldsymbol{I}^-_{\text{sdq}-} + L_{\text{r}} \boldsymbol{I}^-_{\text{rdq}-}. \end{cases} \tag{2}$$

Based on (1) and (2), the dynamics of the DFIG can be expressed as

$$\begin{aligned} \dot{\boldsymbol{I}}^+_{sdq+} = & -\left[\frac{R_s}{\sigma L_s} + j\left(\omega_{\text{pll}+} + \frac{\omega_r L_m^2}{\sigma L_s L_r}\right)\right] \omega_b \boldsymbol{I}^+_{sdq+} \\ & + \frac{\omega_b \boldsymbol{U}^+_{sdq+}}{\sigma L_s} + \left(\frac{R_r}{L_r} - j\omega_r\right) \frac{\omega_b L_m}{\sigma L_s} \boldsymbol{I}^+_{rdq+} \\ & - \frac{\omega_b L_m}{\sigma L_s L_r} \boldsymbol{U}^+_{rdq+} \end{aligned} \tag{3a}$$

$$\begin{aligned} \dot{\boldsymbol{I}}^+_{rdq+} = & \left(\frac{R_s}{L_s} + j\omega_r\right) \frac{\omega_b L_m}{\sigma L_r} \boldsymbol{I}^+_{sdq+} - \frac{\omega_b L_m}{\sigma L_s L_r} \boldsymbol{U}^+_{sdq+} \\ & - \left[\frac{R_r}{\sigma L_r} + j\left(\omega_{\text{pll}+} - \frac{\omega_r}{\sigma}\right)\right] \omega_b \boldsymbol{I}^+_{rdq+} + \frac{\omega_b}{\sigma L_r} \boldsymbol{U}^+_{rdq+} \end{aligned} \tag{3b}$$

$$\begin{aligned} \dot{\boldsymbol{I}}^-_{sdq-} = & -\left[\frac{R_s}{\sigma L_s} + j\left(\frac{\omega_r L_m^2}{\sigma L_s L_r} - \omega_{\text{pll}+}\right)\right] \omega_b \boldsymbol{I}^-_{sdq-} \\ & + \frac{\omega_b \boldsymbol{U}^-_{sdq-}}{\sigma L_s} + \left(\frac{R_r}{L_r} - j\omega_r\right) \frac{\omega_b L_m}{\sigma L_s} \boldsymbol{I}^-_{rdq-} \\ & - \frac{\omega_b L_m}{\sigma L_s L_r} \boldsymbol{U}^-_{rdq-} \end{aligned} \tag{3c}$$

$$\begin{aligned} \dot{\boldsymbol{I}}^-_{rdq-} = & \left(\frac{R_s}{L_s} + j\omega_r\right) \frac{\omega_b L_m}{\sigma L_r} \boldsymbol{I}^-_{sdq-} - \frac{\omega_b L_m}{\sigma L_s L_r} \boldsymbol{U}^-_{sdq-} \\ & - \left[\frac{R_r}{\sigma L_r} - j\left(\omega_{\text{pll}+} + \frac{\omega_r}{\sigma}\right)\right] \omega_b \boldsymbol{I}^-_{rdq-} + \frac{\omega_b}{\sigma L_r} \boldsymbol{U}^-_{rdq-} \end{aligned} \tag{3d}$$

where $\sigma = 1 - L_m^2/(L_s L_r)$.

B. RSC Current Control Model

The current control block diagram of rotor-side converter (RSC) during faults is shown in Fig. 1. According to Fig. 1, the control equation of RSC can be expressed as

$$\begin{cases} \dot{x}_{1+} = I^{*+}_{rd+} - I^+_{rd+} \\ U^+_{rd+} = k_{p1+}\dot{x}_{1+} + k_{i1+}x_{1+} + F_1 \\ \dot{x}_{2+} = I^{*+}_{rq+} - I^+_{rq+} \\ U^+_{rq+} = k_{p2+}\dot{x}_{2+} + k_{i2+}x_{2+} + F_2 \end{cases} \tag{4a}$$

$$\begin{cases} \dot{x}_{1-} = I^{*-}_{rd-} - I^-_{rd-} \\ U^-_{rd-} = k_{p1-}\dot{x}_{1-} + k_{i1-}x_{1-} + F_3 \\ \dot{x}_{2-} = I^{*-}_{rq-} - I^-_{rq-} \\ U^-_{rq-} = k_{p2-}\dot{x}_{2-} + k_{i2-}x_{2-} + F_4 \end{cases} \tag{4b}$$

$$\begin{cases} F_1 = R_r I^+_{rd+} - (\omega_{\text{pll}+} - \omega_r)\sigma L_r I^+_{rq+} + L_m/L_s\,(U^+_{sd+} \\ \quad - R_s I^+_{sd+} + \omega_r L_s I^+_{sq+}) \\ F_2 = R_r I^+_{rq+} + (\omega_{\text{pll}+} - \omega_r)\sigma L_r I^+_{rd+} + L_m/L_s\,(U^+_{sq+} \\ \quad - R_s I^+_{sq+} - \omega_r L_s I^+_{sd+}) \\ F_3 = R_r I^-_{rd-} + (\omega_{\text{pll}+} + \omega_r)\sigma L_r I^-_{rq-} + L_m/L_s\,(U^-_{sd-} \\ \quad - R_s I^-_{sd-} + \omega_r L_s I^-_{sq-}) \\ F_4 = R_r I^-_{rq-} - (\omega_{\text{pll}+} + \omega_r)\sigma L_r I^-_{rd-} + L_m/L_s\,(U^-_{sq-} \\ \quad - R_s I^-_{sq-} - \omega_r L_s I^-_{sd-}) \end{cases}$$

where k_{p1+}, k_{i1+}, k_{p2+}, and k_{i2+} are the proportional and integration coefficients of the PS current loop proportional-integral (PI) controllers of RSC, respectively; and k_{p1-}, k_{i1-}, k_{p2-}, and k_{i2-} are the proportional and integration coefficients of the NS current loop PI controller of RSC, respectively.

C. Grid-Side Converter Model

Generally, the grid-side converter (GSC) is mainly responsible for maintaining the dc-link voltage and dealing with the slip power. During asymmetric faults, the p.u. voltage equations of

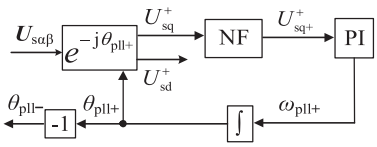

Fig. 3. Control diagram of PLL during asymmetric grid faults.

GSC in the $dq^{\pm}$ frames can be expressed as [24]

$$\begin{cases} \dot{\boldsymbol{I}}^+_{gdq+} = \frac{\omega_b}{L_g}\left(\boldsymbol{U}^+_{sdq+} - R_g\boldsymbol{I}^+_{gdq+} \right. \\ \qquad \left. - j\omega_{\text{pll}+}L_g\boldsymbol{I}^+_{gdq+} - \boldsymbol{V}^+_{gdq+}\right) \\ \dot{\boldsymbol{I}}^-_{gdq-} = \frac{\omega_b}{L_g}\left(\boldsymbol{U}^-_{sdq-} - R_g\boldsymbol{I}^-_{gdq-} \right. \\ \qquad \left. + j\omega_{\text{pll}+}L_g\boldsymbol{I}^-_{gdq-} - \boldsymbol{V}^-_{gdq-}\right). \end{cases} \tag{5}$$

The dc-link voltage control loop and the current control structure of GSC during the asymmetrical FRT are shown in Fig. 1. According to Fig. 1, the control equation of GSC can be expressed as

$$\begin{cases} \dot{x}_{3+} = I^{*+}_{gd+} - I^+_{gd+} \\ V^+_{gd+} = -\left(k_{p3+}\dot{x}_{3+} + k_{i3+}x_{3+}\right) \\ -R_gI^+_{gd+} + \omega_{\text{pll}+}L_gI^+_{gq+} + U^+_{sd+} \\ \dot{x}_{4+} = I^{*+}_{gq+} - I^+_{gq+} \\ V^+_{gq+} = -\left(k_{p4+}\dot{x}_{4+} + k_{i4+}x_{4+}\right) \\ -R_gI^+_{gq+} - \omega_{\text{pll}+}L_gI^+_{gd+} + U^+_{sq+} \end{cases} \tag{6a}$$

$$\begin{cases} \dot{x}_{3-} = I^{*-}_{gd-} - I^-_{gd-} \\ V^-_{gd-} = -\left(k_{p3-}\dot{x}_{3-} + k_{i3-}x_3\right) \\ -R_gI^-_{gd-} - \omega_{\text{pll}+}L_gI^-_{gq-} + U^-_{sd-} \\ \dot{x}_{4-} = I^{*-}_{gq-} - I^-_{gq-} \\ V^-_{gq-} = -\left(k_{p4-}\dot{x}_{4-} + k_{i4-}x_{4-}\right) \\ -R_gI^-_{gq-} + \omega_{\text{pll}+}L_gI^-_{gd-} + U^-_{sq-} \end{cases} \tag{6b}$$

$$\begin{cases} \dot{x}_5 = U^{*+}_{\text{dc}+} - U^+_{\text{dc}+} \\ I^{*+}_{gd+} = k_{p5+}\dot{x}_5 + k_{i5+}x_5 \\ \dot{U}^+_{\text{dc}+} = \frac{1}{CU^+_{\text{dc}+}}(U^+_{sd+}I^+_{gd+} \\ + U^+_{sq+}I^+_{gq+} + U^-_{sd-}I^-_{gd-} + U^-_{sq-}I^-_{gq-}) \\ -\frac{1}{CU^+_{\text{dc}+}}(U^+_{rd+}I^+_{rd+} + U^+_{rq+}I^+_{rq+} + U^-_{rd-}I^-_{rd-} + U^-_{rq-}I^-_{rq-}) \end{cases} \tag{6c}$$

where k_{p3+}, k_{i3+}, k_{p4+}, and k_{i4+} are the proportional and integration coefficients of the PS current loop PI controllers of GSC, respectively; and k_{p3-}, k_{i3-}, k_{p4-}, and k_{i4-} are the proportional and integration coefficients of the NS current loop PI controllers of GSC, respectively. k_{p5+} and k_{i5+} are the proportional and integration coefficients of the dc-link voltage control loop PI controllers of GSC, respectively. V_g represents the output voltage vector of the GSC inverter.

D. PLL Model

In order to accurately obtain the phase and the frequency of the PS voltage during the FRT, a notch filter (NF) with center frequency $2\omega_{1+}$ is used to filter out the NS voltage [25], as shown in Fig. 3.

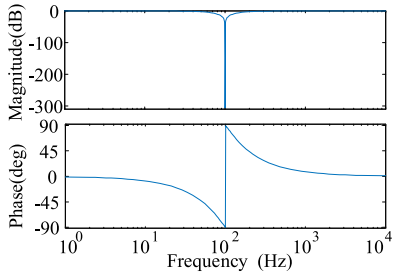

Fig. 4. Bode diagram of NF.

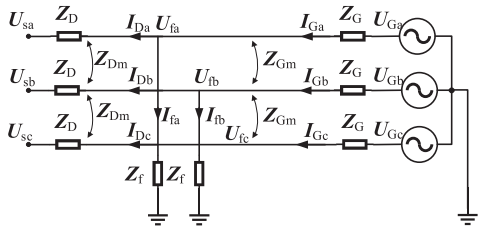

Fig. 5. Equivalent circuit of the two-phase ground fault.

$\theta_{\text{pll}-}$ is the angle difference between the d^--axis of the dq^- reference frame and α-axis of the $\alpha\beta$ stationary frame. According to [26], the model can be simplified when $\theta_{\text{pll}-}$ is equal to $-\theta_{\text{pll}+}$. Thus, in order to simplify the analysis, the $dq^{\pm}$ reference frames adopted in this article are consistent with that in [26]. As a result, $\theta_{\text{pll}-}$ is replaced by $-\theta_{\text{pll}+}$.

Fig. 4 shows the bode diagram of the NF under asymmetric faults. It can be seen that the NF has a large negative gain at $2\omega_{1+}$, where $\omega_{1+} = 50$ Hz. Therefore, it is assumed that the NS voltage can be completely filtered out by NF.

According to Figs. 2 and 3, the PLL can be described as

$$\begin{cases} \dot{\theta}_{\text{pll}+} = \omega_b\omega_{\text{pll}+} \\ \dot{x}_6 = U^+_{sq+} \\ \omega_{\text{pll}+} = k_{p6+}U^+_{sq+} + k_{i6+}x_6 \end{cases} \tag{7}$$

where k_{p6+} and k_{i6+} are the proportional and integration coefficients of PLL's PI controller, respectively.

E. Power Grid Model

During asymmetric faults, the PS and NS impedances of the power grid are coupled. Therefore, in order to accurately describe the dynamics of the power grid, it is necessary to build the asymmetric fault network model. In this article, a two-phase ground fault is taken as an example, as shown in Fig. 5.

It is assumed that the three-phase transmission lines are completely transposed and the interaction between the faulty branches is ignored [27]. According to Fig. 5, it can be obtained by Kirchhoff's and Ohm's laws

$$\begin{cases} \boldsymbol{U}^T_{\text{Gabc}} - \boldsymbol{U}^T_{\text{fabc}} = \boldsymbol{Z}^m_{\text{G}}\boldsymbol{I}^T_{\text{Gabc}} \\ \boldsymbol{U}^T_{\text{fabc}} - \boldsymbol{U}^T_{\text{sabc}} = \boldsymbol{Z}^m_{\text{D}}\boldsymbol{I}^T_{\text{Dabc}} \\ \boldsymbol{I}^T_{\text{Gabc}} = \boldsymbol{I}^T_{\text{Dabc}} + \boldsymbol{I}^T_{\text{fabc}} \\ \boldsymbol{I}^T_{\text{fabc}} = \boldsymbol{G}^m_{\text{f}}\boldsymbol{U}^T_{\text{fabc}} \end{cases} \tag{8}$$

where $\boldsymbol{Z}_G^m = \begin{bmatrix} \boldsymbol{Z}_G & \boldsymbol{Z}_{Gm} & \boldsymbol{Z}_{Gm} \\ \boldsymbol{Z}_{Gm} & \boldsymbol{Z}_G & \boldsymbol{Z}_{Gm} \\ \boldsymbol{Z}_{Gm} & \boldsymbol{Z}_{Gm} & \boldsymbol{Z}_G \end{bmatrix}$; $\boldsymbol{Z}_{\mathrm{D}}^m = \begin{bmatrix} \boldsymbol{Z}_{\mathrm{D}} & \boldsymbol{Z}_{\mathrm{Dm}} & \boldsymbol{Z}_{\mathrm{Dm}} \\ \boldsymbol{Z}_{\mathrm{Dm}} & \boldsymbol{Z}_{\mathrm{D}} & \boldsymbol{Z}_{\mathrm{Dm}} \\ \boldsymbol{Z}_{\mathrm{Dm}} & \boldsymbol{Z}_{\mathrm{Dm}} & \boldsymbol{Z}_{\mathrm{D}} \end{bmatrix}$; $\mathbf{G}_f^m = \begin{bmatrix} 1/\boldsymbol{Z}_f & 0 & 0 \\ 0 & 1/\boldsymbol{Z}_f & 0 \\ 0 & 0 & 0 \end{bmatrix}$; $\boldsymbol{Z}_G$ and $\boldsymbol{Z}_{Gm}$ are the line self-impedance and mutual impedance between the fault point and the power grid, respectively; $\boldsymbol{Z}_D$ and $\boldsymbol{Z}_{Dm}$ are the line self-impedance and mutual impedance between the point of common coupling (PCC) point and the fault point, respectively; and $\boldsymbol{Z}_f$ is the ground impedance of the fault phase.

Based on (8), the relationship between $\boldsymbol{U}_{Gabc}$ and $\boldsymbol{U}_{sabc}$ can be expressed as

$$\begin{aligned} \boldsymbol{U}_{\mathrm{sabc}}^T = & \underbrace{\left(\boldsymbol{Z}_{\mathrm{G}}^m \boldsymbol{G}_{\mathrm{f}}^m + \mathbf{E}\right)^{-1}}_{\boldsymbol{H}_{\mathrm{G}}^m} \boldsymbol{U}_{\mathrm{Gabc}}^T \\ & - \underbrace{\left[\boldsymbol{Z}_D^m + \left(\boldsymbol{Z}_{\mathrm{G}}^m \boldsymbol{G}_{\mathrm{f}}^m + E\right)^{-1} \boldsymbol{Z}_{\mathrm{G}}^m\right]}_{\boldsymbol{Z}_{\mathrm{DT}}^m} \boldsymbol{I}_{\mathrm{Dabc}}^T \end{aligned} \tag{9}$$

where $\boldsymbol{E}$ is the identity matrix.

According to the symmetrical component method, (9) can be decomposed into the following expression:

$$\begin{bmatrix} U_{sa+} \\ U_{sa-} \\ U_{sa0} \end{bmatrix} = \boldsymbol{H}_{G\pm0}^m \begin{bmatrix} U_{Ga+} \\ U_{Ga-} \\ U_{Ga0} \end{bmatrix} - \boldsymbol{Z}_{DT\pm0}^m \begin{bmatrix} I_{Da+} \\ I_{Da-} \\ I_{Da0} \end{bmatrix} \tag{10}$$

where

$$\boldsymbol{T} = \begin{bmatrix} 1 & 1 & 1 \\ a^2 & a & 1 \\ a & a^2 & 1 \end{bmatrix}; a = -1/2 + j\sqrt{3}/2$$

$$\boldsymbol{H}_{G\pm0}^m = \boldsymbol{T}^{-1} \boldsymbol{H}_G^m \boldsymbol{T}; \boldsymbol{Z}_{DT\pm0}^m = \boldsymbol{T}^{-1} \boldsymbol{Z}_{DT}^m \boldsymbol{T}.$$

The DFIG system is connected to the power grid by a three-phase three-wire system, there is no zero-sequence component flow path. Therefore, the zero-sequence component is ignored, and only the 2×2 matrices in the upper left corner of the $\boldsymbol{H}_{G\pm0}^m$ and $\boldsymbol{Z}_{DT\pm0}^m$ are retained as

$$\begin{bmatrix} U_{\mathrm{sa}+} \\ U_{\mathrm{sa}-} \end{bmatrix} = \boldsymbol{H}_{\mathrm{G}\pm}^m \begin{bmatrix} U_{\mathrm{Ga}+} \\ U_{\mathrm{Ga}-} \end{bmatrix} - \boldsymbol{Z}_{\mathrm{DT}\pm}^m \begin{bmatrix} I_{\mathrm{Da}+} \\ I_{\mathrm{Da}-} \end{bmatrix} \tag{11}$$

where $\boldsymbol{H}_{G\pm}^m = \begin{bmatrix} \boldsymbol{H}_{g11} & \boldsymbol{H}_{g12} \\ \boldsymbol{H}_{g21} & \boldsymbol{H}_{g22} \end{bmatrix}$; and $\boldsymbol{Z}_{DT\pm}^m = \begin{bmatrix} Z_{dt11} & Z_{dt12} \\ Z_{dt21} & Z_{dt22} \end{bmatrix}$.

For the convenience of subsequent calculations, $\boldsymbol{Z}_{dt11}$–$\boldsymbol{Z}_{dt22}$ and $\boldsymbol{H}_{g11}$–$\boldsymbol{H}_{g22}$ are rewritten as follows:

$$\begin{bmatrix} \boldsymbol{Z}_{dt11} & \boldsymbol{Z}_{dt12} \\ \boldsymbol{Z}_{dt21} & \boldsymbol{Z}_{dt22} \end{bmatrix} = \begin{bmatrix} R_{DT11} + pL_{DT11} & R_{DT12} + pL_{DT12} \\ R_{DT21} + pL_{DT21} & R_{DT22} + pL_{DT22} \end{bmatrix} \tag{12a}$$

$$\begin{bmatrix} \boldsymbol{H}_{g11} & \boldsymbol{H}_{g12} \\ \boldsymbol{H}_{g21} & \boldsymbol{H}_{g22} \end{bmatrix} = \begin{bmatrix} R_{G11} + pL_{G11} & R_{G12} + pL_{G12} \\ R_{G21} + pL_{G21} & R_{G22} + pL_{G22} \end{bmatrix}. \tag{12b}$$

According to the space-vector synthesis method [28], (11) can be transformed into the vector form in the stationary system as follows:

$$\begin{bmatrix} \boldsymbol{H}_{g11} \boldsymbol{U}_{G+} \\ \boldsymbol{H}_{g21} \boldsymbol{U}_{G+} \end{bmatrix} = \begin{bmatrix} \boldsymbol{U}_{s+} \\ \boldsymbol{U}_{s-}^c \end{bmatrix} + \begin{bmatrix} \boldsymbol{Z}_{dt11} & \boldsymbol{Z}_{dt12} \\ \boldsymbol{Z}_{dt21} & \boldsymbol{Z}_{dt22} \end{bmatrix} \begin{bmatrix} \boldsymbol{I}_{D+} \\ \boldsymbol{I}_{D-}^c \end{bmatrix}. \tag{13}$$

It can be seen from (13) that under asymmetric faults, since the elements of the auxiliary diagonal in the impedance matrix are not zero, there is a coupling between the PS and NS voltages and currents due to the asymmetry of line structure. According to (13), the PS and NS voltage and current vectors can be projected in the $dq^{\pm}$ reference frames, respectively, as shown

$$\begin{cases} \boldsymbol{U}_{sdq+}^+ = \boldsymbol{H}_{G11} \boldsymbol{U}_{Gdq+}^+ - \boldsymbol{Z}_{DT11} \boldsymbol{I}_{Ddq+}^+ \\ -\boldsymbol{Z}_{DT12} I_{Ddq-}^{c-} - \frac{L_{DT11}}{\omega_b} \dot{\boldsymbol{I}}_{Ddq+}^+ - \frac{L_{DT12}}{\omega_b} \dot{\boldsymbol{I}}_{Ddq-}^{c-} \\ \boldsymbol{U}_{sdq-}^- = \boldsymbol{H}_{G21}^c \boldsymbol{U}_{Gdq+}^{c+} - \boldsymbol{Z}_{DT21}^c \boldsymbol{I}_{Ddq+}^{c+} \\ -\boldsymbol{Z}_{DT22}^c \boldsymbol{I}_{Ddq-}^- - \frac{L_{DT21}}{\omega_b} \dot{\boldsymbol{I}}_{Ddq+}^{c+} - \frac{L_{DT22}}{\omega_b} \dot{\boldsymbol{I}}_{Ddq-}^- \end{cases} \tag{14}$$

where $\begin{bmatrix} \boldsymbol{Z}_{DT11} & \boldsymbol{Z}_{DT12} \\ \boldsymbol{Z}_{DT21} & \boldsymbol{Z}_{DT22} \end{bmatrix} = \begin{bmatrix} R_{DT11} + j\omega_{\mathrm{pll}} L_{DT11} & R_{DT12} + j\omega_{\mathrm{pll}} L_{DT12} \\ R_{DT21} + j\omega_{\mathrm{pll}} L_{DT21} & R_{DT22} + j\omega_{\mathrm{pll}} L_{DT22} \end{bmatrix}$; and $\begin{bmatrix} \boldsymbol{H}_{G11} \\ \boldsymbol{H}_{G21} \end{bmatrix} = \begin{bmatrix} R_{G11} + j\omega_{\mathrm{pll}} L_{G11} \\ R_{G21} + j\omega_{\mathrm{pll}} L_{G21} \end{bmatrix}$.

Similarly, combined with the symmetric component method and the space-vector synthesis method, the relationship between the fault point voltage and the PCC voltage can be expressed as

$$\begin{bmatrix} \boldsymbol{U}_{f+} \\ \boldsymbol{U}_{f-} \end{bmatrix} = \begin{bmatrix} \boldsymbol{U}_{s+} \\ \boldsymbol{U}_{s-} \end{bmatrix} + \begin{bmatrix} \boldsymbol{Z}_{d11} & 0 \\ 0 & \boldsymbol{Z}_{d22} \end{bmatrix} \begin{bmatrix} \boldsymbol{I}_{D+} \\ \boldsymbol{I}_{D-} \end{bmatrix} \tag{15}$$

where $\boldsymbol{Z}_{d11}$ and $\boldsymbol{Z}_{d22}$ are the PS and NS impedances between the fault point and PCC, respectively; $\boldsymbol{Z}_{d11} = \boldsymbol{Z}_{d22} = \boldsymbol{Z}_D$-$\boldsymbol{Z}_{Dm}$. For the convenience of subsequent calculations; and $\boldsymbol{Z}_{d11}$ and $\boldsymbol{Z}_{d22}$ can be rewritten as $\boldsymbol{Z}_{d11} = R_{D11} + pL_{D11}$ and $\boldsymbol{Z}_{d22} = R_{D22} + pL_{D22}$.

According to (15), the PS and NS voltage and current vectors can be projected in the $dq^{\pm}$ reference frames, respectively

$$\begin{cases} \boldsymbol{U}_{sdq+}^+ = \boldsymbol{U}_{fdq+}^+ - Z_{D11} \boldsymbol{I}_{Ddq+}^+ - \frac{L_{D11}}{\omega_b} \dot{\boldsymbol{I}}_{Ddq+}^+ \\ \boldsymbol{U}_{sdq-}^- = \boldsymbol{U}_{fdq-}^- - \boldsymbol{Z}_{D22} \boldsymbol{I}_{Ddq-}^- - \frac{L_{D11}}{\omega_b} \dot{\boldsymbol{I}}_{Ddq-}^- \end{cases} \tag{16}$$

where $\boldsymbol{Z}_{D11} = R_{D11} + j\omega_{\mathrm{pll}} L_{D11}$ and $\boldsymbol{Z}_{D22} = R_{D22}$-$j\omega_{\mathrm{pll}} L_{D22}$. In addition, according to Fig. 1 and Kirchhoff's current law, the out current of PCC can be expressed as

$$\begin{cases} \boldsymbol{I}_{Ddq+}^+ = \boldsymbol{I}_{sdq+}^+ + \boldsymbol{I}_{gdq+}^+ + j\omega_{\mathrm{pll}+} C_f \boldsymbol{U}_{sdq+}^+ + \frac{C_f}{\omega_b} \dot{\boldsymbol{U}}_{sdq+}^+ \\ \boldsymbol{I}_{Ddq-}^- = \boldsymbol{I}_{sdq-}^- + \boldsymbol{I}_{gdq-}^- - j\omega_{\mathrm{pll}+} C_f \boldsymbol{U}_{sdq-}^- + \frac{C_f}{\omega_b} \dot{\boldsymbol{U}}_{sdq-}^- \end{cases}. \tag{17}$$

Based on (1)–(7), (14), (16), and (17), the interaction relationship between the DFIG system and the power grid during asymmetrical FRT can be obtained, as shown in Fig. 6.

It is clear from Fig. 6 that the PS and NS current controllers' response is influenced by the PLL's dynamics, and the injected current from DFIG into the power grid can be further influenced through (17). And then, $\boldsymbol{U}_{sdq\pm}^{\pm}$ can be affected by $\boldsymbol{I}_{Ddq\pm}^{\pm}$ through (14) and (16). In addition, the outputs of PLL will be influenced again due to varying $\boldsymbol{U}_{sdq\pm}^{\pm}$. It can be seen that as the interface between the wind power generation system and the power grid, PLL has an important effect on the interaction between DFIG and the power grid. The interaction may deteriorate the dynamic stability of the DFIG system during asymmetric faults. Therefore, the dynamic stability of the DFIG system under the asymmetric faults should be further investigated.

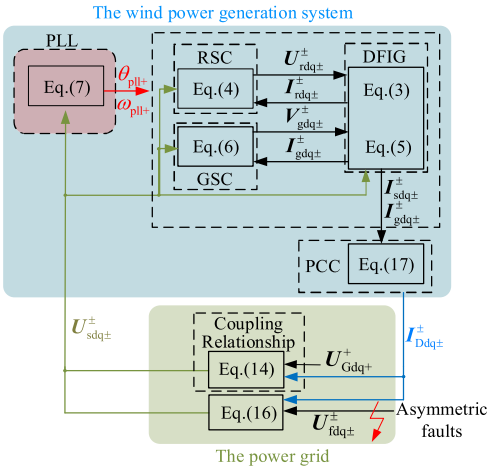

Fig. 6. Interaction relationship between the wind power generation system and the power grid during asymmetric faults.

TABLE I
EIGENVALUES ANALYSIS RESULTS OF DFIG SYSTEM UNDER FAULTS

Dominated unstable Eigenvalues		Damping ratio	Dominant state variables	Participation factors
$\lambda_{1,2}$	38.09±457.37i	-0.0833	ΔI^{+}_{sd+}, ΔI^{+}_{sq+}	0.06, 0.09
			ΔI^{-}_{sd-}, ΔI^{-}_{sq-}	0.07, 0.10
			ΔI^{+}_{rd+}, ΔI^{+}_{rq+}	0.06, 0.11
			ΔI^{-}_{rd-}, ΔI^{-}_{rq-}	0.07, 0.10
			$\Delta\theta_{\mathrm{pll}+}$	0.28

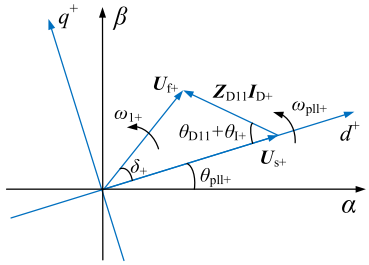

Fig. 7. Space-vector relationship diagram between the PCC voltage and fault point voltage.

III. Stability Analysis During Asymmetric Faults and Optimal Current Control Reference Algorithm

A. Modal Analysis

To analyze the dynamic stability of the DFIG system, the small-signal state-space model is established first. Linearizing (1)–(7), (14), (16), and (17), the small-signal state-space functions of the DFIG system during asymmetric faults can be expressed as

$$\begin{cases} \Delta\dot{\boldsymbol{x}} = \boldsymbol{A}\Delta\boldsymbol{x} + \boldsymbol{B}\Delta\boldsymbol{u} \\ 0 = \boldsymbol{C}\Delta\boldsymbol{x} + \boldsymbol{D}\Delta\boldsymbol{u} \end{cases} \tag{18}$$

where $\Delta\boldsymbol{x}$ is the state variable; $\Delta\boldsymbol{u}$ is the control variable; $\Delta\boldsymbol{x} = [\Delta\boldsymbol{I}^{\pm}_{sdq\pm}\ \Delta\boldsymbol{I}^{\pm}_{rdq\pm}\ \Delta x_{1\pm}\ \Delta x_{2\pm}\ \Delta\boldsymbol{I}^{\pm}_{Ddq\pm}\ \Delta\boldsymbol{U}^{\pm}_{sdq\pm}\ \Delta\boldsymbol{I}^{\pm}_{gdq\pm}\ \Delta x_{3\pm}\ \Delta x_{4\pm}\ \Delta U_{\mathrm{dc}}\ \Delta x_5\ \Delta\theta_{\mathrm{pll}+}\ \Delta x_6]^T$; and $\Delta\boldsymbol{u} = [\Delta\boldsymbol{U}^{\pm}_{rdq\pm}\ \Delta\boldsymbol{V}^{\pm}_{gdq\pm}\ \Delta\omega_{\mathrm{pll}+}]^T$. The detailed derivation of the small-signal state-space model is given in the Appendix.

By solving (18), the system's dominant oscillation modes and its corresponding participation factors can be determined. In addition, the concept of the voltage unbalance factors ε is introduced to measure the degree of the asymmetric faults [29], which is defined as $\varepsilon = |\boldsymbol{U}^{-}_{sdq-}|/|\boldsymbol{U}^{+}_{sdq+}|$. Moreover, SCR is introduced to measure the strength of the system. The calculation of SCR is defined as follows:

$$\mathrm{SCR} = \frac{S_{\mathrm{PCC}}}{P_{\mathrm{rated}}} = \frac{S_{\mathrm{PCC}}Z_L}{U^2_{\mathrm{rated}}} = \frac{1}{Z^*_L} \tag{19}$$

where the S_{PCC} is the short-circuit capacity at the PCC; P_{rated} is the rated power of the DFIG, and U_{rated} is the ac rated voltage; and Z_L is the transmission line's impendence. Z^*_L is the p.u. value of the transmission line's impendence, when $\varepsilon = 0.67$, SCR $= 2$. The participation factors of the dominant state variables and the damping ratio of the dominated unstable eigenvalues are given in Table I.

Table I only lists the state variables with the participation factor greater than 0.05. It can be seen from Table I that during asymmetric faults, the DFIG system has the risk of instability. The dominant unstable eigenvalues of the DFIG system are affected by the PLL and current control loops during faults, in which the PLL is the dominant factor. This is consistent with the previous analysis. Therefore, this article focuses on improving the stability of the system from the perspective of PLL. What is more, in the PLL control time scale (about 100–500 ms), the current can track its reference value instantaneously due to the much higher bandwidths of ac current controls [30], so the dynamic of current control loops (less than 100 ms) will be ignored in the following analysis.

It can be seen from Fig. 6 that the total output PS and NS currents of the DFIG system will affect the PLL, and then the dynamic of the system will be further influenced. What is more, from the existing work, it can be seen that optimizing the total output current reference values of the DFIG system can help to improve the stability of the system. From the perspective of small-signal stability, the injection of the d-axis current can significantly improve the damping of the system [11]. In addition, from the perspective of large disturbance stability, the injection of the d-axis current during the fault can also increase the stability margin of the system and reduce the risk of the instability of the system [31]. However, Liu *et al.* [11] and Pei *et al.* [31] both focus on improving the stability of the DFIG system under the symmetric grid fault. Considering that the probability of asymmetric faults is much higher than that of the symmetric fault, improving the stability of the system by optimizing the total output current reference values of the DFIG system during the asymmetric faults is an issue worthy of attention. The influence of the PS and NS current references on the stability of the system needs to be further analyzed.

B. Influence of PS and NS Current References on Stability

Assuming the voltage amplitude at the fault point will not change during the fault duration stage, the vector diagram of the terminal voltage and fault point voltage is given in Fig. 7.

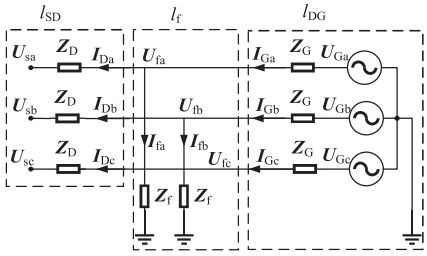

Fig. 8. Three parts of the equivalent circuit of the two-phase ground fault.

According to Fig. 7, (7) can be rewritten as

$$\begin{cases} \dot{\delta}_+ = \omega_{1+} - \omega_{\text{pll}+} \\ \dot{x}_6 = U^+_{sq+} \\ \omega_{\text{pll}+} = K_{p6+}U^+_{sq+} + K_{i6+}x_6 \end{cases} \tag{20}$$

where δ_+ is the angle difference between $\boldsymbol{U}_{f+}$ and $\boldsymbol{U}_{s+}$.

In addition, from Fig. 7, it can be concluded that the projection of $\boldsymbol{U}_{s+}$ on the q^+-axis is

$$U^+_{sq+} = \boldsymbol{U}_{f+}\sin\delta_+ - \boldsymbol{Z}_{D11}\boldsymbol{I}_{D+}\sin(\theta_{D11} + \theta_{I+}) \tag{21}$$

where θ_{I+} is the angle between $\boldsymbol{I}_{D+}$ and d^+; θ_{D11} is the impedance angle of $\boldsymbol{Z}_{D11}$.

According to the modal analysis, the current control loop has less influence on the system stability than PLL. To simplify the analysis, it is assumed that the feedback value of the current control loop during faults can follow the reference. In addition, when the fault point and the fault degree are determined, $\boldsymbol{Z}_{D11}$ and $\boldsymbol{I}_{D+}$ can be regarded as constants. Therefore, according to (20) and (21), the small-signal state-space functions can be expressed as

$$\begin{bmatrix} \Delta\dot{x}_6 \\ \Delta\dot{\delta}_+ \end{bmatrix} = \begin{bmatrix} 0 & \boldsymbol{U}_{f+}\cos\delta_{0+} \\ -K_{i6+} & -K_{p6+}\boldsymbol{U}_{f+}\cos\delta_{0+} \end{bmatrix} \begin{bmatrix} \Delta x_6 \\ \Delta\delta_+ \end{bmatrix}. \tag{22}$$

Based on (22), the damping ratio ξ_+ can be expressed as

$$\xi_+ = \frac{K_{p6+}}{2}\sqrt{\frac{\boldsymbol{U}_{f+}\cos\delta_{0+}}{K_{i6+}}}. \tag{23}$$

It can be seen from (23) that the damping ratio ξ_+ can reach the maximum when $\delta_{0+} = 0$, which means that the system has the highest small-signal stability. Therefore, in order to improve the dynamic stability of the system, it is necessary to reduce δ_+. It can be seen from Fig. 6 that $\boldsymbol{U}^{\pm}_{sdq\pm}$ is influenced by $\boldsymbol{I}^{\pm}_{Ddq\pm}$, which means δ_+ will be affected by $\boldsymbol{I}^{\pm}_{Ddq\pm}$. The relationship among PS, NS currents, and δ_+ during asymmetric faults will be analyzed in detail as follows.

In order to further explain the coupling relationship between the PS and NS voltages and currents under asymmetric faults and study the influence of PS and NS currents on δ_+, the network model of the circuit is decomposed into three parts, l_{SD}, l_{DG}, and l_f, as shown in Fig. 8.

Ignoring the dynamic of the current loops and combining with symmetric component method and space-vector synthesis method, it can be obtained

$$\begin{bmatrix} \boldsymbol{U}_{\text{G}+} \\ \boldsymbol{U}_{\text{G}-} \end{bmatrix} = \begin{bmatrix} \boldsymbol{U}_{\text{f}+} \\ \boldsymbol{U}_{\text{f}-} \end{bmatrix} + \boldsymbol{Z}_{\text{G}\pm} \begin{bmatrix} \boldsymbol{I}_{\text{G}+} \\ \boldsymbol{I}_{\text{G}-} \end{bmatrix} = \begin{bmatrix} \boldsymbol{U}_{\text{f}+} \\ \boldsymbol{U}_{\text{f}-} \end{bmatrix} + \begin{bmatrix} \boldsymbol{Z}_{\text{G}11} & 0 \\ 0 & \boldsymbol{Z}_{\text{G}22} \end{bmatrix} \begin{bmatrix} \boldsymbol{I}_{\text{G}+} \\ \boldsymbol{I}_{\text{G}-} \end{bmatrix} \tag{24a}$$

$$\begin{cases} \boldsymbol{I}_{\text{f}+} = G_{11}\boldsymbol{U}_{\text{f}+} + G_{12}\boldsymbol{U}^c_{\text{f}-} \\ \boldsymbol{I}_{\text{f}-} = G_{21}\boldsymbol{U}^c_{\text{f}+} + G_{22}\boldsymbol{U}_{\text{f}-} \end{cases}, G_\pm = \begin{bmatrix} G_{11} & G_{12} \\ G_{21} & G_{22} \end{bmatrix} \tag{24b}$$

$$\begin{bmatrix} \boldsymbol{I}_{\text{G}+} \\ \boldsymbol{I}_{\text{G}-} \end{bmatrix} = \begin{bmatrix} \boldsymbol{I}_{\text{f}+} \\ \boldsymbol{I}_{\text{f}-} \end{bmatrix} + \begin{bmatrix} \boldsymbol{I}_{\text{D}+} \\ \boldsymbol{I}_{\text{D}-} \end{bmatrix} \tag{24c}$$

where $G_\pm = [T^{-1}G^m_f T]_{2\times2}$ and $Z_{G\pm} = [T^{-1}Z^m_G T]_{2\times2}$. The subscript 2×2 represents the 2×2 matrix in the upper left corner. Combining (24) with (16), the PS and NS network models of the system under asymmetric faults expressed by vectors can be obtained, as shown in Fig. 9(a). It can be seen from Fig. 9(a) that the PS and NS networks of l_{SD} and l_{DG} are decoupled. However, due to the asymmetric line structure l_f, there is a coupling relationship between the PS and NS networks. Therefore, the interaction between five networks in Fig. 9(a) should be considered, and the system exhibits the characteristic of multiple inputs and multiple outputs during the asymmetric faults. By contrast, during the symmetric fault, there is no NS network and coupling network. Moreover, l_{DG} is ignored and only the PS network of l_{SD} is considered. As a result, the system exhibits the characteristic of single-input and single-output during the symmetric fault.

Combine (14) with (16), Fig. 9(a) can be converted to Fig. 9(b). In order to consider all coupling relationships, superimpose the conjugate of the second equation in (14) on the first equation in (14) and it can be obtained

$$\begin{aligned} (\boldsymbol{H}_{G11}+\boldsymbol{H}_{G21})\,\boldsymbol{U}_{G+} = \boldsymbol{U}_{s+} + \boldsymbol{U}^c_{s-} + (\boldsymbol{Z}_{DT11}+\boldsymbol{Z}_{DT21})\,\boldsymbol{I}_{D+} \\ + (\boldsymbol{Z}_{DT12}+\boldsymbol{Z}_{DT22})\,\boldsymbol{I}^c_{D-}. \end{aligned} \tag{25}$$

According to the previous analysis, δ_+ is related to $\boldsymbol{U}_{s+}$. Therefore, in order to eliminate $\boldsymbol{U}^c_{s-}$, substitute the conjugate of the second equation of (16) on (25), and the simplified equivalent coupling relationship between the PS and NS voltage and current vectors can be obtained

$$\begin{aligned} \boldsymbol{U}_{H+} - \boldsymbol{U}_{s+} = (Z_{DT11}+Z_{DT21})\,\boldsymbol{I}_{D+} \\ + (\boldsymbol{Z}_{DT12}+\boldsymbol{Z}_{DT22}-\boldsymbol{Z}^c_{D22})\,\boldsymbol{I}^c_{D-} \end{aligned} \tag{26}$$

where $\boldsymbol{U}_{H+} = (\boldsymbol{H}_{G11}+\boldsymbol{H}_{G21})\boldsymbol{U}_{G+} - \boldsymbol{U}^c_{f-}$. $\boldsymbol{U}_{H+}$ can be regarded as the generalized grid voltage during the asymmetric faults.

In addition, the relationship between the simplified equivalent coupling network and $\boldsymbol{U}_{s+}$ can be obtained and Fig. 9(b) can be converted to Fig. 9(c). It can be seen from Fig. 9(c) that the five networks are simplified as two networks. Moreover, $\boldsymbol{U}_{s+}$ is affected by both networks, which means δ_+ is affected by both $\boldsymbol{I}_{D+}$ and $\boldsymbol{I}_{D-}$.

Combined with the grid code, the DFIG system should inject PS reactive power to increase the PS voltage and absorb NS reactive power to reduce the NS voltage. The PS reactive current I_{DQ+} should satisfy $\Delta I_{DQ+} = k_+\,\Delta U_{s+}$, and the NS reactive

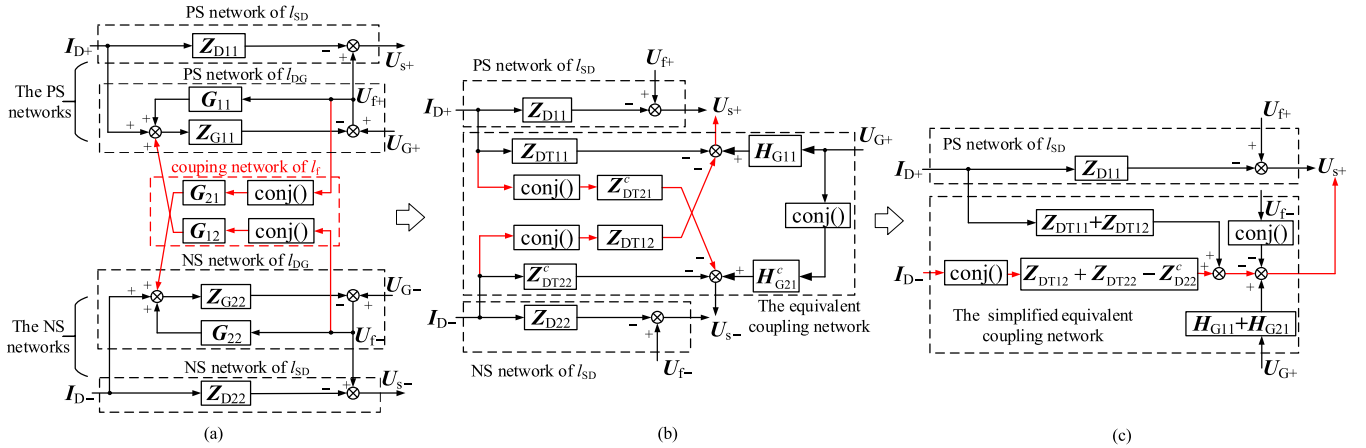

Fig. 9. Networks under the asymmetric fault. (a) PS and NS networks of the system. (b) Equivalent coupling network of the system. (c) Simplified equivalent coupling network of the system.

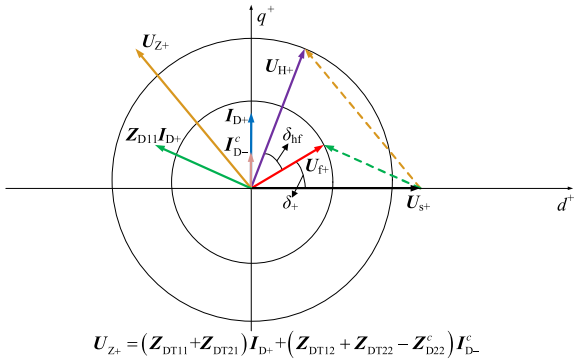

Fig. 10. Vector relationship diagram among $\boldsymbol{U}_{H+}$, $\boldsymbol{U}_{f+}$, and $\boldsymbol{U}_{s+}$ when the DFIG only injects PS and NS q-axis current.

current I_{DQ-} should satisfy $\Delta I_{DQ-} = k_- \Delta U_{s-}$ [16], where k_+ and k_- are the PS and NS reactive current gains, respectively. In this article, $\boldsymbol{I}^+_{q+}$ is equal to I_{DQ+}. In addition, the NS voltage vector can be obtained in the dq^- reference frame, and the corresponding $\boldsymbol{I}_{DQ-}$ can also be calculated. I^-_{q-} is equal to the projection of $\boldsymbol{I}_{DQ-}$ on the q^--axis. It should be noted that from the perspective of power control, I^-_{q-} can only control a part of the NS reactive power by this way. If the requirement of the grid code is needed to be fully satisfied and the NS reactive power is controlled accurately by I^-_{q-}, U^-_{q-} is required to be adjusted to zero. Accordingly, the NS reference frame will be different, which will increase the complexity of the model. However, the focus of the following study in this article is to optimize the d-axis components of currents to improve the stability of the system. Therefore, in order to simplify the analysis, the optimal PS and NS d-axis components of currents are derived based on the reference frames shown in Fig. 2.

Combining (16) with (26), the vector relationship among $\boldsymbol{U}_{H+}$, $\boldsymbol{U}_{f+}$, and $\boldsymbol{U}_{s+}$ can be obtained when the DFIG system only injects PS and NS q-axis currents into the power grid, as shown in Fig. 10, where δ_{hf} represents the angle difference between $\boldsymbol{U}_{f+}$ and $\boldsymbol{U}_{H+}$. Assuming the grid voltage and the voltage at the fault point will not change during the fault, when the fault position and fault degree are determined, the magnitude of $\boldsymbol{U}_{f+}$ and $\boldsymbol{U}_{H+}$ and the phase difference between them remain unchanged, which means that δ_{hf} is a constant.

It can be seen from Fig. 10 that two vector circles should be added in the dq^+ reference frames during the asymmetric faults. One of them is the track of $\boldsymbol{U}_{f+}$, which can reflect the effect of the PS network of l_{SD} on δ_+, while the other is the track of $\boldsymbol{U}_{H+}$, which can reflect the effect of the simplified equivalent coupling network on δ_+.

According to Fig. 10, the q-axis component of $\boldsymbol{U}_{f+}$ in the PLL frame can be expressed as

$$U^+_{\mathrm{fq+}} = R_{\mathrm{D11}} I^+_{\mathrm{Dq+}} + X_{\mathrm{D11}} I^+_{\mathrm{Dd+}} \tag{27a}$$

$$U^+_{\mathrm{fq+}} = U_{\mathrm{f+}} \sin \delta_+. \tag{27b}$$

Substitute (27a) into (27b), and the relationship between δ_+ and PS current can be obtained

$$\delta_+ = \arcsin\left(\frac{R_{D11} I^+_{Dq+} + X_{D11} I^+_{Dd+}}{U_{f+}}\right). \tag{28}$$

It can be seen from (28) that when δ_+ is constant, there is a coupling relationship between I^+_{Dd+} and I^+_{Dq+}. In addition, the q-axis component of $\boldsymbol{U}_{H+}$ in the PLL frame can be expressed as

$$U^+_{\mathrm{Hq+}} = K_1 I^+_{\mathrm{Dq+}} + K_2 I^+_{\mathrm{Dd+}} + K_3 I^-_{\mathrm{Dd-}} + K_4 I^-_{\mathrm{Dq-}} \tag{29a}$$

$$U^+_{Hq+} = U_{H+} \sin(\delta_{hf} + \delta_+) \tag{29b}$$

where $\begin{cases} K_1 = R_{\mathrm{DT11}} + R_{\mathrm{DT21}} \\ K_2 = X_{\mathrm{DT11}} + X_{\mathrm{DT21}} \\ K_3 = X_{\mathrm{DT12}} + X_{\mathrm{DT22}} - X_{\mathrm{D22}} \\ K_4 = -R_{\mathrm{DT12}} - R_{\mathrm{DT22}} + R_{\mathrm{D22}} \end{cases}$. Substitute (29a) into (29b), and the relationship among δ_+, PS, and NS current can be obtained

$$\delta_+ = \arcsin \frac{K_1 I^+_{Dq+} + K_2 I^+_{Dd+} + K_3 I^-_{Dd-} + K_4 I^-_{Dq-}}{U_{H+}} - \delta_{hf} \tag{30}$$

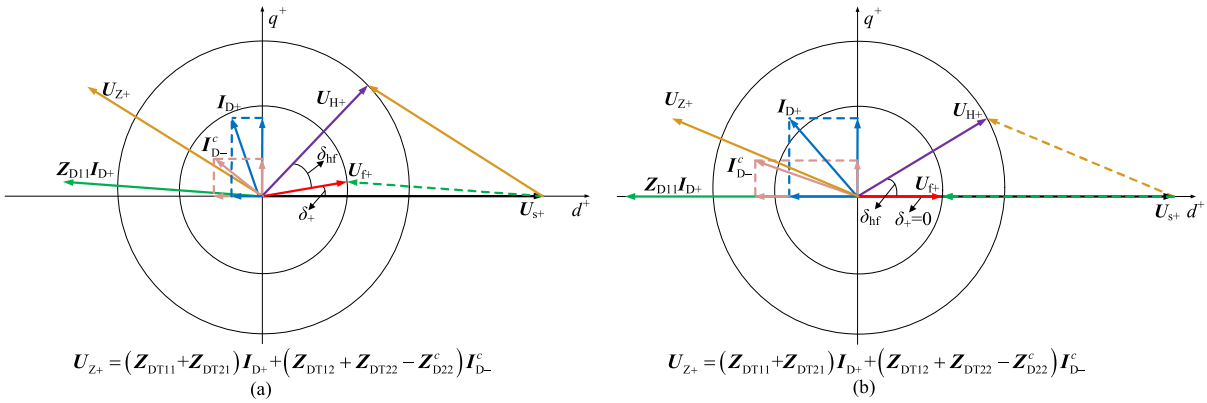

Fig. 11. Vector relationship diagram. (a) δ_+ is reduced when the DFIG simultaneously outputs PS d-axis, NS d-axis, and PS q-axis current and absorbs NS q-axis current. (b) $\delta_+ = 0$ when the DFIG simultaneously outputs optimal PS d-axis, NS d-axis, and PS q-axis current and absorbs NS q-axis current.

where δ_+ can be accessed by (28) or (30), and the two values obtained by (28) and (30), respectively, should be equal to each other. Therefore, combine (28) with (30) and it can be obtained

$$I^-_{Dd-} = \frac{U_{H+}\sin(\delta_{hf} + \arcsin(\frac{R_{D11}I^+_{Dq+}+X_{D11}I^+_{Dd+}}{U_{f+}}))}{K_3} - \frac{K_1 I^+_{Dq+}+K_2 I^+_{Dd+} + K_4 I^-_{Dq-}}{K_3} \tag{31}$$

where I^+_{Dq+} and I^-_{Dq-} are determined. In addition, when the grid fault position is determined, K_1–K_4 are constant. What is more, U_{f+}, U_{H+}, and δ_{hf} are not changed during the fault duration stage. Therefore, there is a coupling relationship between I^+_{Dd+} and I^-_{Dd-} during asymmetric faults, as shown in (31).

As mentioned above, there are two inherent coupling relationships, which need to be satisfied by controlling the dq-axis components of PS and NS currents in the system during the asymmetric faults, as shown in (28) and (31). In addition, according to the previous analysis, the system stability reaches the highest when $\delta_+ = 0$. Therefore, the specific coupling relationships and the optimal PS and NS d-axis current reference values for $\delta_+ = 0$ will be further derived as follows.

It can be seen from Fig. 11(a) that δ_+ can be reduced by injecting the d-axis current, which means that the stability of the system will be improved. When $\delta_+ = 0$, the vector relationship is shown in Fig. 11(b). In this case, the PS and NS d-axis currents are defined as the optimal PS and NS d-axis current $I^+_{Dd\_opt+}$ and $I^-_{Dd\_opt-}$, respectively. Combined with (28), $I^+_{Dd\_opt+}$ can be obtained as

$$I^+_{Dd\_opt+} = -\frac{R_{D11}}{X_{D11}} I^+_{Dq+}. \tag{32}$$

Substitute (32) into (31), and $I^-_{Dd\_opt-}$ can further be derived as

$$I^-_{Dd\_opt-} = \frac{U_{H+}\sin\delta_{hf} - K_1 I^+_{Dq+} - K_2 I^+_{Dd\_opt+} - K_4 I^-_{Dq-}}{K_3}. \tag{33}$$

Therefore, the optimal PS and NS d-axis current reference values can be obtained as

$$\begin{cases} I^{*+}_{Dd+} = I^+_{Dd\_opt+} \\ I^{*-}_{Dd-} = I^-_{Dd\_opt-}. \end{cases} \tag{34}$$

In general, when δ_+ is constant, there is a coupling relationship between I^+_{Dd+} and I^+_{Dq+}, as shown in (28), and at the same time, there is another coupling relationship between I^+_{Dd+} and I^-_{Dd-}, as shown in (31), during asymmetric faults. When $\delta_+ = 0$, the damping ratio of PLL is the highest and the system has the optimal small-signal stability with $I^+_{Dd+} = I^+_{Dd\_opt+}$ and $I^-_{Dd-} = I^-_{Dd\_opt-}$. It is worth noting that the PS d-axis current reference shown in (34) is the same as the result derived from [11], which indicates that the symmetric fault is a special case of the asymmetric faults, and the algorithm proposed in this article is more universal.

In addition, it is needed to be emphasized that the expressions of optimal PS and NS d-axis current derived in this article are only applicable to the PS and NS reference frames shown in Fig. 2. The optimal d-axis current reference values are derived from the mathematical model of the power grid. If different reference frames are adopted, the expressions of the model of the power grid and the corresponding optimal d-axis current reference values will be different. In general, the research ideas and analysis methods of this article about the optimal d-axis currents can be used as a reference.

C. PS and NS d-Axis Current Matching Scheme Considering the Current Capacity Limitation of DFIG

It should be noted that the ability of DFIG to output the current is limited by its capacity, i.e.,

$$\sqrt{(I^+_{Dd+})^2 + (I^+_{Dq+})^2} + \sqrt{(I^-_{Dd-})^2 + (I^-_{Dq-})^2} \le I_M \tag{35}$$

where I_M is the maximum current capacity of the DFIG-based WT. It can be seen that when the total current demand exceeds the limit, four current control variables need to be reallocated during the asymmetric faults, which is more complicated than that during the symmetric fault. The PS and NS currents reallocation method will be analyzed as follows.

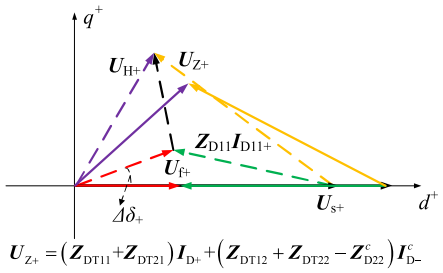

Fig. 12. Vector relationship diagram when the *d*-axis current is reduced.

Substitute (34) into (35), if the required optimal current, which makes $\delta_+ = 0$, exceeds the capacity limit of DFIG-based WT, the system has to reallocate the *d*-axis current. In this case, the PS and NS *q*-axis currents are set first combined with the grid codes, and the remaining current capacity is allocated to the PS and NS *d*-axis currents. It will be discussed in detail as follows.

According to the above-mentioned analysis, I^{*-}_{Dd-} is derived from (31) combining with I^{*+}_{Dd+}, therefore, I^{*+}_{Dd+} needs to be determined first. Assuming that $I^{*+}_{Dd+} = I^{+}_{Dd\_opt+-} \ \Delta I^{+}_{Dd+}$, where ΔI^{+}_{Dd+} is the reduction of the PS *d*-axis current. According to (28), δ_+ will change as the PS *d*-axis current changes. As shown in Fig. 12, when the PS *d*-axis current decreases, the positional relationship among the vectors changes from solid lines to dashed lines.

As a result, δ_+ increases $\Delta\delta_+$, which means that the system stability gets worse when the PS *d*-axis current is reduced. When $\Delta\delta_+$ is very small, linearize (28) at the equilibrium point of the system, and $\Delta\delta_+$ can be expressed as

$$\Delta\delta_+ = \frac{X_{D11}\Delta I^{+}_{Dd+}}{U_{f+}}. \tag{36}$$

From (36), it can be seen that $\Delta\delta_+$ is directly proportional to ΔI^{+}_{Dd+}, that is, the more the PS *d*-axis current decreases, the more δ_+ deviates from the optimal value, which means that the stability of the system is worse. Therefore, under the premise that the total capacity does not exceed the limit, ΔI^{+}_{Dd+} should be as small as possible to improve the system stability.

In order to find the ΔI^{+}_{Dd+} that meets the above-mentioned requirements, the PS and NS current distribution problem considering the capacity limitation can be described as a nonlinear programming problem with constraints, where the independent variable is ΔI^{+}_{Dd+}, the objective function is to find the minimum $\Delta\delta_+$, and the constraint condition is the current capacity limit. Therefore, the mathematical model is shown as

$$\begin{aligned} &\min f(x) \\ &\text{s.t.} \begin{cases} g(x) = 0 \\ x > 0 \end{cases} \end{aligned} \tag{37}$$

where

$$x = \Delta I^{+}_{Dd+}$$

$$f(x) = \Delta\delta_+ = \frac{X_{D11}}{U_{f+}}x;$$

$$g(x) = \sqrt{\left(I^{+}_{Dd\_opt+} - x\right)^2 + \left(I^{*+}_{Dq+}\right)^2} + \sqrt{\left(I^{*-}_{Dd-}\right)^2 + \left(I^{*-}_{Dq-}\right)^2} - I_M.$$

Equation (37) can be solved by constructing a penalty function and combining it with intelligent optimization algorithms [32]. ΔI^{+}_{Dd+} is obtained by solving (37), and then I^{*+}_{Dd+} and I^{*-}_{Dd-} can further be calculated. Therefore, when the current capacity exceeds the limit, the PS and NS *d*-axis current reference values are shown as

$$\begin{cases} I^{*+}_{Dd+} = I^{+}_{Dd\_opt+} - \Delta I^{+}_{Dd+}, \\ \qquad \text{where } \Delta I^{+}_{Dd+} \text{is caculated by (37)} \\ I^{*-}_{Dd-} = \dfrac{U_{H+}\sin\left(\delta_{hf}+\arcsin\left(\frac{R_{D11}I^{*+}_{Dq+}+X_{D11}I^{*+}_{Dd+}}{U_{f+}}\right)\right)}{K_3} \\ -\dfrac{K_1 I^{*+}_{Dq+}+K_2 I^{*+}_{Dd+}+K_4 I^{*-}_{Dq-}}{K_3}. \end{cases} \tag{38}$$

D. Optimal Current Control Reference Algorithm During Asymmetrical FRT

It can be seen from the above-mentioned analysis that the small-signal stability of the DFIG system can be enhanced by injecting the PS and NS *d*-axis currents into the power grid during the faults. Considering the current capacity limitation of DFIG-based WT, the specific optimal control scheme is as follows.

1) During asymmetric faults, the PS and NS *q*-axis currents are given combined with the grid codes.
2) The remaining current capacity of DFIG-based WT is used to output PS and NS *d*-axis currents, as follows.
   a) Scheme 1: When the total current demand does not exceed the current capacity limitation of DFIG-based WT, the optimal PS and NS *d*-axis currents will be output according to (34).
   b) Scheme 2: When the total current demand is greater than the current capacity limitation of DFIG-based WT, it is necessary to reallocate the *d*-axis currents, and the system outputs PS and NS *d*-axis currents according to (38).

The block diagram of the optimal current control reference algorithm during asymmetrical FRT is shown in Fig. 13.

It is worth noting that this algorithm is an adaptive algorithm. Under different asymmetric fault conditions, as long as the required grid fault information is accessed, the corresponding optimal current reference values can be automatically calculated. Therefore, the algorithm can apply to different grid faults. Moreover, the parameters required by the algorithm can be obtained based on measurable data and existing fault location algorithms. For example, in [33], based on the modal analysis and *RL* model of the transmission line, an accurate time-domain algorithm for fault location using one-terminal data is presented. Combining with voltages and currents at the measurement point, the fault distance, the fault impedance, and the source parameters at the remote end can be solved as the unknown variables of the system model. Therefore, the transmission line impedance $\boldsymbol{Z}_G$ and $\boldsymbol{Z}_D$ and the fault impedance $\boldsymbol{Z}_f$ can be obtained. What is more, the fault location accuracy of the method proposed in [33] is not

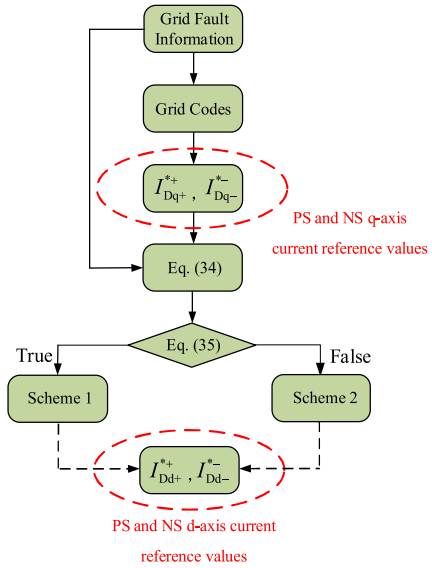

Fig. 13. Optimal current control reference algorithm during asymmetrical FRT.

affected by fault type, fault impedance, system operation mode, and network configuration. Because the fault location is not the focus of this article, a detailed investigation will not be carried out. As a consequence, the algorithm proposed in [33] can be directly adopted to achieve the necessary fault parameters in the proposed scheme.

In general, based on the interaction mechanism between the power grid and the wind power generation system, this article proposes a PS and NS current control reference optimization algorithm. By optimizing the current control references, the output angle of the PLL can be adjusted, which can make the system operate at a stable operating point with high damping and can significantly improve the small-signal stability of the system. Compared with the previous control strategies for improving the system stability during asymmetric faults, the algorithm proposed in this article has the following advantages.

1) It is an adaptive algorithm. Under different asymmetric faults, when the grid fault information is determined, the optimal current control references can be automatically calculated. Therefore, the algorithm can apply to different fault conditions.
2) The optimal current references can be calculated online based on the required parameters, which can be obtained by the real-time measurable data. Therefore, it is not necessary to obtain the state of the DFIG system during the fault and the algorithm does not rely on the mathematical model of the DFIG system, which enhances the practicability of the algorithm.
3) It can clearly explain the mechanism for improving the stability of the system. What is more, the coupling relationship between PS and NS voltages and currents caused by the interaction between the power grid and DFIG system is considered in the algorithm.

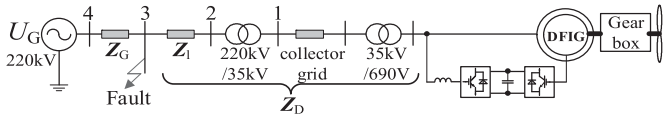

Fig. 14. Aggregated wind power plant and Thevenin equivalent grid for simulation studies.

TABLE II
CURRENT DEMAND AND THE STATOR VOLTAGE THD DURING FAULTS OF THE THREE SCHEMES IN CASE 1

Control Scheme	I^{*+}_{Dd+}, I^{*+}_{Dq+}	I^{*-}_{Dd-}, I^{*-}_{Dq-}	Total Current	THD (%)
Traditional Scheme	0 p.u. 0.675 p.u.	0 p.u. -0.3 p.u.	0.98 p.u.	10.11%
Scheme 1	-0.12 p.u. 0.675 p.u.	-0.35 p.u. -0.3 p.u.	1.17 p.u.	0.68%
Scheme 2	-0.05 p.u. 0.675 p.u.	-0.18 p.u. -0.3 p.u.	1.00 p.u.	1.57%

IV. SIMULATION AND EXPERIMENTAL VALIDATIONS

A. Simulation Validations

In order to verify the correctness of the proposed improved control scheme, the simulation model is built in MATLAB/Simulink. The simulated system was configured, as shown in Fig. 14 and the detailed parameters of the system are given in the Appendix. The wind farm consists of 75 × 2 MW DFIG-based WTs, which are aggregated into a single DFIG [34]. It is connected to the power grid via a step-up transformer and high-voltage cable. The two-phase ground fault happens on bus 3. The two-phase ground fault is discussed as an example and the results under other types of asymmetrical faults also exhibit a similar phenomenon.

1) Case 1: Table II lists the current demand and the total harmonic distortion (THD) of stator B-phase voltage during faults when adopting the traditional control scheme, Schemes 1 and 2, respectively, when the SCR = 2, the PS grid voltage drops to 0.45 p.u. and $\varepsilon = 0.67$.

Fig. 15(a) shows the simulation results of the traditional control scheme in Case 1. It can be seen that the DFIG system has oscillation instability during asymmetric faults under the weak grid, which is consistent with the analysis results. Fig. 15(a)(v) is the discrete Fourier transform (DFT) result of the stator B-phase voltage. From the analysis results of DFT, it can be seen that the THD of the stator voltages during the traditional control scheme is 10.11%. In addition, it can be seen from Fig. 15(a)(v) that the stator voltages contain the oscillation components at 27, 73, 127, 273, and 327 Hz. Among them, 73 Hz is the dominant oscillation frequency and the rest are the coupling frequency components [19]. Furthermore, the unbalanced input voltages or impedances create the NS fundamental component in the stator voltages,

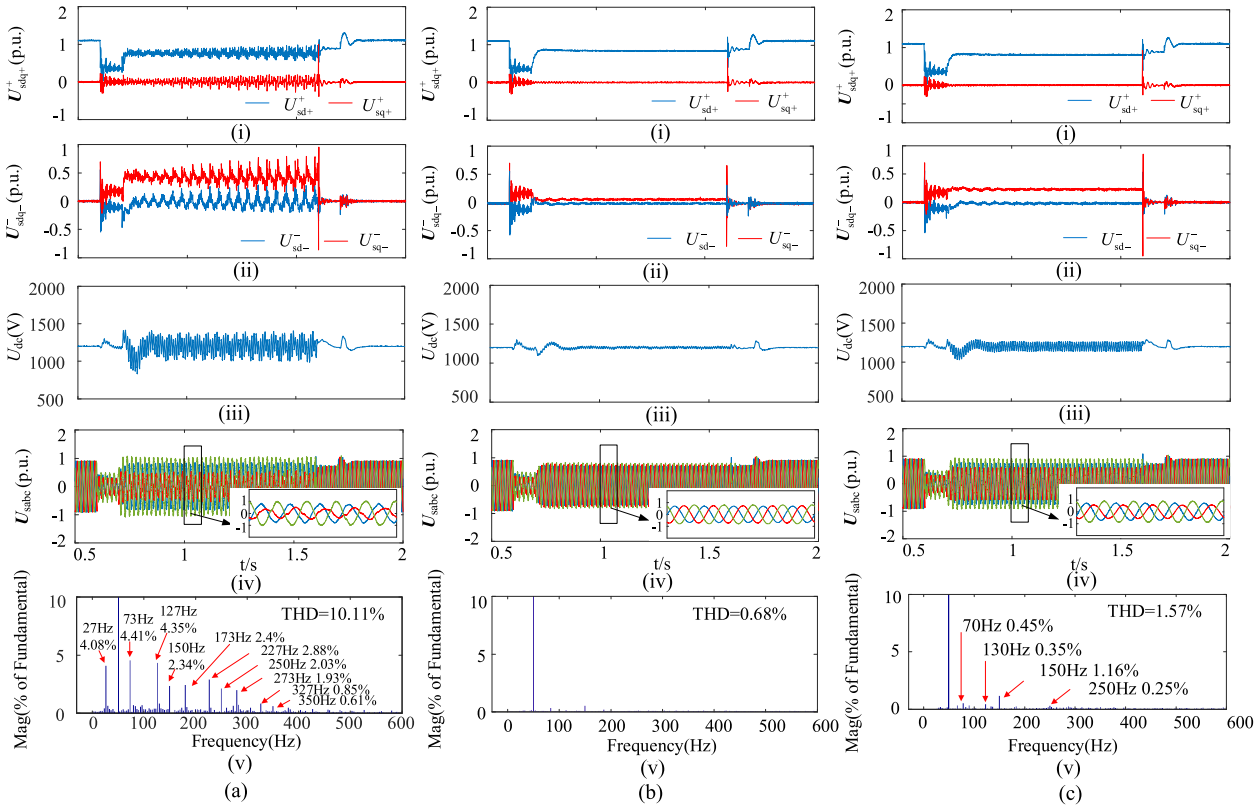

Fig. 15. Simulation results in Case 1. (a) Traditional scheme (b) Scheme 1. (c) Scheme 2. (i) U^{+}_{sd+} and U^{+}_{sq+}. (ii) U^{-}_{sd-} and U^{-}_{sq-}. (iii) $U_{\rm dc}$. (iv) Stator three-phase voltage $\boldsymbol{U}_{sabc}$. (v) DFT analysis of stator B-phase voltage.

which also causes 150, 250, and 350 Hz coupling frequency components according to Liu *et al.* [19].

Fig. 15(b) shows the simulation results when the DFIG system outputs the optimal PS and NS *d*-axis currents according to Scheme 1 during asymmetric grid faults. The THD of stator B-phase voltage is reduced to 0.68%, as shown in Fig. 15(b)(v). It can be seen that the stability of the DFIG system can be significantly improved by adopting Scheme 1, which is consistent with the theoretical analysis. In addition, Scheme 1 can effectively suppress the NS voltage and reduce the overvoltage risk of the nonfault phase, as shown in Fig. 15(b)(ii) and (iv). However, it can be seen from Table II that although the THD of the optimal Scheme 1 is the minimum, the total current demand of Scheme 1 exceeds the current capacity limit of DFIG-based WT. Therefore, according to the proposed optimal control scheme, it is necessary to switch to Scheme 2. Fig. 15(c) shows the simulation results when Scheme 2 is adopted. Compared with Fig. 15(b) and (c), it can be seen that both Schemes 1 and 2 can effectively enhance the small-signal stability of the DFIG system during grid faults. Since the PS and NS *d*-axis current reference values in Scheme 2 are less than the optimal values so that $\Delta\delta+ > 0$, when Scheme 2 is adopted, the stability of the system should be weaker than that when adopting Scheme 1. Moreover, the THD of Scheme 2 is also greater than the THD of Scheme 1, as given in Table II, which is consistent with the previous theory analysis. Furthermore, the THD of Scheme 1 or 2 is smaller than that of the traditional control scheme, which fully verifies the effectiveness of the optimal current control algorithm.

TABLE III
CURRENT DEMAND AND THE STATOR VOLTAGE THD DURING FAULTS OF THE THREE SCHEMES IN CASE 2

Control Scheme	I^{*+}_{Dd+}, I^{*+}_{Dq+}	I^{*-}_{Dd-}, I^{*-}_{Dq-}	Total Current	THD (%)
Traditional Scheme	0 p.u. 0.6 p.u.	0 p.u. -0.25 p.u.	0.85 p.u.	13.23%
Scheme 1	-0.106 p.u. 0.6 p.u.	-0.42 p.u. -0.25 p.u.	1.1 p.u.	0.9%
Scheme 2	-0.04 p.u. 0.6 p.u.	-0.317 p.u. -0.25 p.u.	1.00 p.u.	1.53%

2) Case 2: Fig. 16 shows the simulation results when SCR = 1.5. In this case, the PS grid voltage drops to 0.5 p.u. and $\varepsilon = 0.5$. Table III lists the current demand and the THD of stator B-phase voltage during faults when adopting the traditional control scheme and Schemes 1 and 2.

The simulation results when adopting the traditional control scheme and Schemes 1 and 2 in Case 2 are shown in Fig. 16. It can be seen from Fig. 16(a) that the DFIG system has oscillation

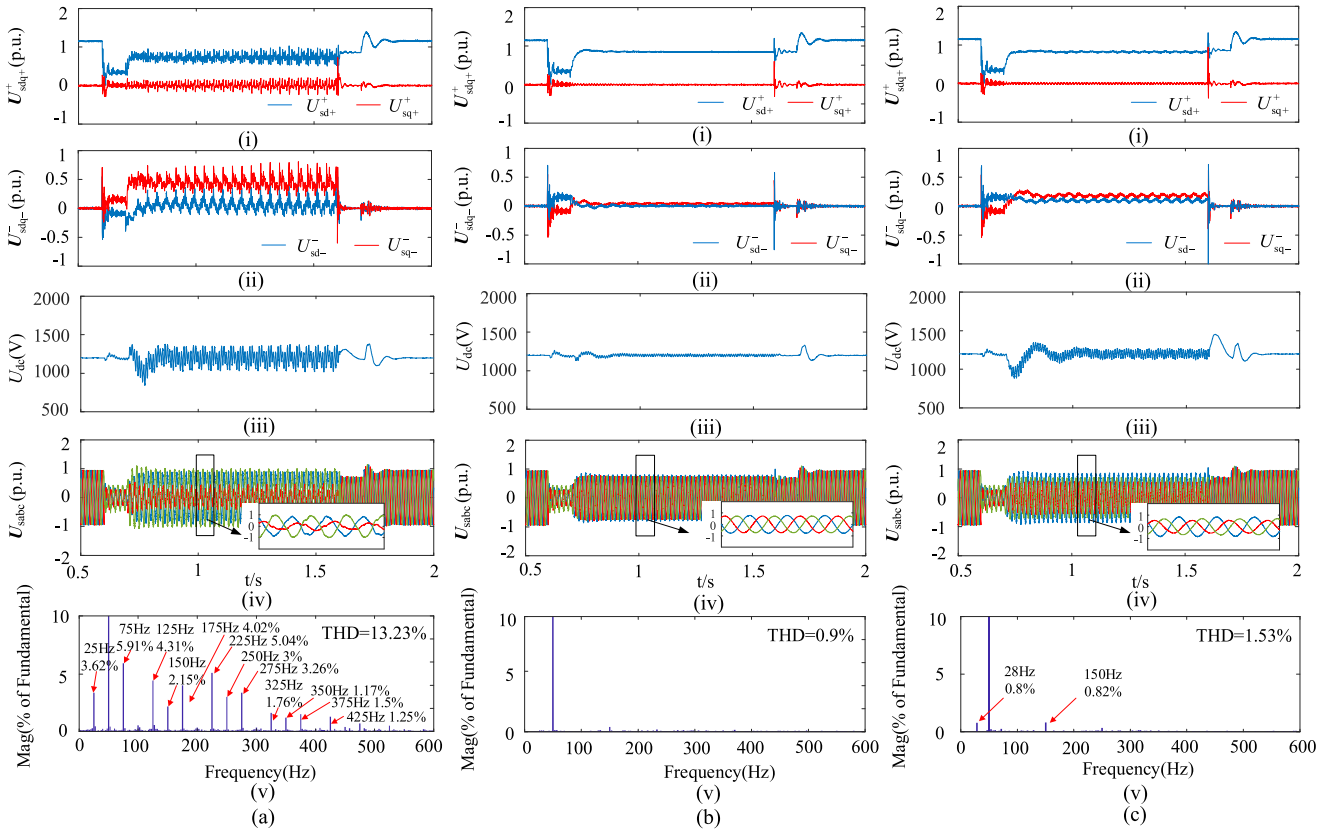

Fig. 16. Simulation results in Case 2. (a) Traditional Scheme. (b) Scheme 1. (c) Scheme 2. (i) U^{+}_{sd+} and U^{+}_{sq+}. (ii) U^{-}_{sd-} and U^{-}_{sq-}. (iii) $U_{\rm dc}$. (iv) Stator three-phase voltage $\boldsymbol{U}_{sabc}$. (v) DFT analysis of stator B-phase voltage.

TABLE IV
CURRENT DEMAND AND THE STATOR VOLTAGE THD DURING FAULTS OF THE THREE SCHEMES IN CASE 3

Control Scheme	I^{*+}_{Dd+}, I^{*+}_{Dq+}	I^{*-}_{Dd-}, I^{*-}_{Dq-}	Total Current	THD (%)
Traditional Scheme	0 p.u. 0.45 p.u.	0 p.u. -0.24 p.u.	0.69 p.u.	12.69%
Scheme 1	-0.08 p.u. 0.45 p.u.	-0.45 p.u. -0.24 p.u.	0.97 p.u.	0.85%

instability during asymmetric faults under the weak grid. The THD of the stator voltages when adopting the traditional control scheme is 13.23%. What is more, the oscillation components confirm to the frequency coupling characteristic. Fig. 16(b) and (c) shows the simulation results when adopting Schemes 1 and 2, respectively. It can be seen that Scheme 1 can suppress the oscillation of the system more effectively than Scheme 2. In addition, the THD of Scheme 2 is also greater than the THD of Scheme 1, as given in Table III, which is consistent with the theory analysis. Furthermore, the THD of Scheme 1 or 2 is smaller than that of the traditional control scheme, which fully verifies the effectiveness of the optimal current control algorithm.

3) CASE 3: Fig. 17 shows the simulation results when the PS grid voltage drops to 0.6 p.u. In this case, SCR $= 2$ and $\varepsilon = 0.4$. Table IV displays the current demand and the THD of stator B-phase voltage during faults when adopting the traditional control scheme and Scheme 1. Scheme 2 is not adopted because the total current demand of Scheme 1 does not exceed the current capacity limit of DFIG-based WT.

The simulation results when adopting the traditional control scheme and Scheme 1 in Case 3 are shown in Fig. 17. It can be seen from Fig. 17(a) that the DFIG system has a small-signal instability during asymmetric faults. The THD of the stator voltages during the traditional control scheme is 12.69%. Moreover, the oscillation components confirm the frequency coupling characteristic. Fig. 17(b) shows the simulation results when adopting Scheme 1. It can be seen that Scheme 1 can significantly improve the small-signal stability of the system. What is more, the THD of Scheme 1 is also smaller than that of the traditional control scheme, which verifies the effectiveness of the optimal current control algorithm again.

B. Experimental Validations

In order to further validate the correctness of the stability analysis of the DFIG system during asymmetric fault conditions, the experimental platform based on DSP TMS320F28335 was built, as shown in Fig. 18. The detailed parameters of the experimental

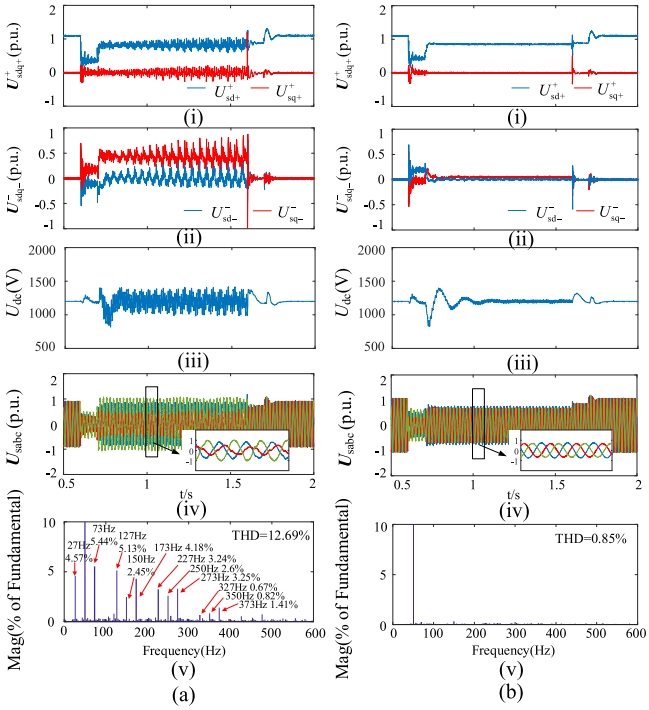

Fig. 17. Simulation results in Case 3. (a) Traditional Scheme. (b) Scheme 1. (i) U^{+}_{sd+} and U^{+}_{sq+}. (ii) U^{-}_{sd-} and U^{-}_{sq-}. (iii) $U_{\rm dc}$. (iv) Stator three-phase voltage $\boldsymbol{U}_{sabc}$. (v) DFT analysis of stator B-phase voltage.

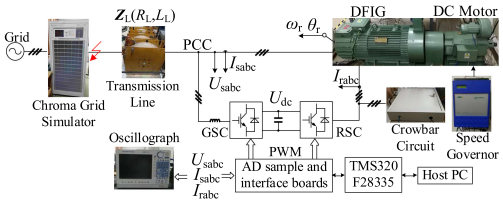

Fig. 18. Schematic diagram of the experimental system.

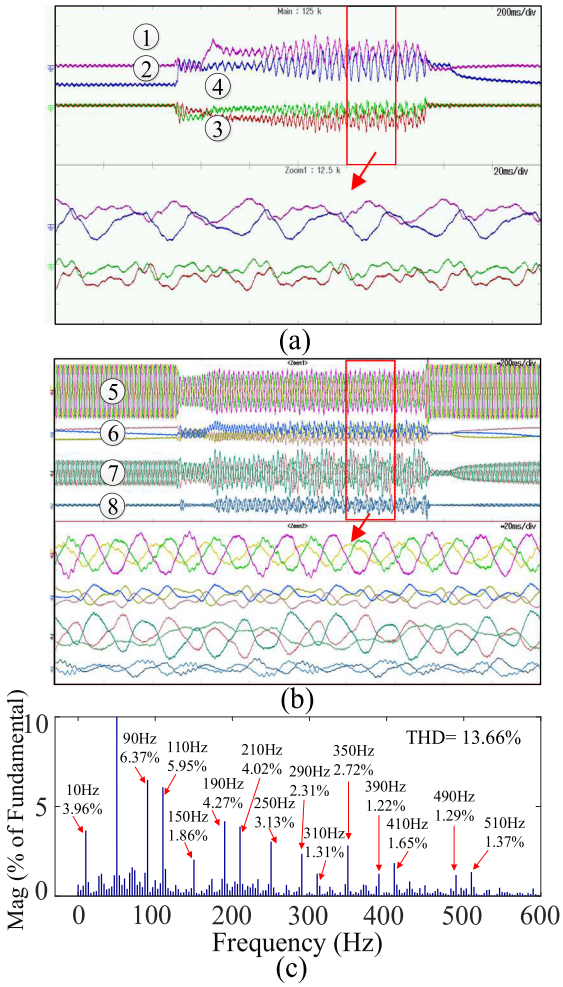

Fig. 19. Experimental results when adopting the traditional scheme. (a) ① and ②: I^{+}_{sd+} and I^{+}_{sq+} (0.85 p.u./div); ③ and ④: I^{-}_{sd-} and I^{-}_{sq-} (0.85 p.u./div). (b) ⑤: stator three-phase voltage $\boldsymbol{U}_{sabc}$ (0.91 p.u./div); ⑥: rotor three-phase current $\boldsymbol{I}_{rabc}$ (1.49 p.u./div); ⑦: stator three-phase current $\boldsymbol{I}_{sabc}$ (1.49 p.u./div); ⑧: GSC two-phase current $\boldsymbol{I}_{gab}$ (1.49 p.u./div). (c) DFT analysis of stator B-phase voltage.

system are given in the Appendix. The DFIG system is driven by a dc motor and the line impedance is simulated by air-core reactors. The two-phase fault of the power grid is generated by using the Chroma 61830 grid simulator. The SCR of the system is 2.3.

Fig. 19 shows the experimental waveforms adopting the traditional control scheme when the PS grid voltage drops to 0.47 p.u. and the $\varepsilon = 0.64$. In Fig. 19, the system outputs the PS q-axis current of 0.645 p.u. and absorbs the NS q-axis current of 0.3 p.u. It can be seen that the DFIG system exhibits the dynamic instability phenomenon during the severe asymmetric faults, which is consistent with the analysis results. Fig. 19(c) shows the DFT analysis results of the stator B-phase voltage. According to the DFT analysis results, the THD of stator voltage with the traditional control scheme is 13.66%. Furthermore, it can be seen from Fig. 19(c) that the stator voltages include the oscillation components at 10, 90, 110, 190, 210, 290, 310, 390, 410, 490, and 510 Hz. Among them, the 90 Hz is the dominant oscillation frequency, and the rest are the coupling frequency components. In addition, the unbalanced grid voltages also produce 150, 250, and 350 Hz coupling frequency components in the stator voltages.

Fig. 20 shows the experimental waveforms adopting Schemes 1 and 2, respectively. In Fig. 20(A), when PS and NS q-axis currents are determined combined with the grid codes, the DFIG system outputs the PS d-axis current of 0.147 p.u. and NS d-axis current of 0.29 p.u. according to Scheme 1. It can be seen that the oscillation of the DFIG system during asymmetric faults under the weak grid is suppressed and the DFIG system achieves a successful LVRT, which conforms to the theoretical analysis. Fig. 20(A-c) shows the DFT analysis results of the stator B-phase voltage. The THD of stator voltage is reduced to 3.70%. The oscillation components at 10, 90, 110 Hz, and so on are almost eliminated. Furthermore, the 150, 250, and 350 Hz voltage components are also suppressed. As the NS grid voltage is existing during the fault, the 150, 250, and 350 Hz voltage components could not be mitigated to zero. As can be

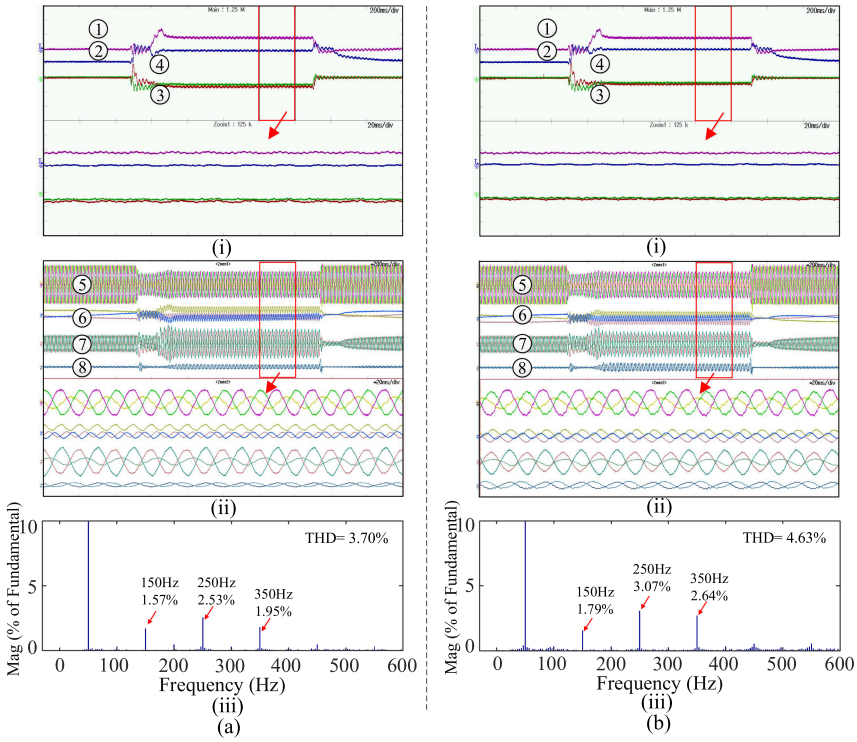

Fig. 20. Experimental results. (a) Scheme 1. (b) Scheme 2. ① and ②: I^{+}_{sd+} and I^{+}_{sq+} (0.85 p.u./div); ③ and ④: I^{-}_{sd-} and I^{-}_{sq-} (0.85 p.u./div); ⑤: stator three-phase voltage $\boldsymbol{U}_{sabc}$ (0.91 p.u./div); ⑥: rotor three-phase current $\boldsymbol{I}_{rabc}$ (1.49 p.u./div); ⑦: stator three-phase current $\boldsymbol{I}_{sabc}$ (1.49 p.u./div); ⑧: GSC two-phase current $\boldsymbol{I}_{gab}$ (1.49 p.u./div); (iii): DFT analysis of stator B-phase voltage.

seen from the experiment results and above-mentioned analysis, it further indicates that the dynamic stability of the DFIG system can be significantly enhanced during severe asymmetric faults by adopting the proposed Scheme 1.

When the total current of Scheme 1 exceeds the current capacity limit of DFIG-based WT, it is necessary to switch to Scheme 2. Fig. 20(b) shows the experimental results when Scheme 2 is adopted. In this case, the DFIG system outputs 0.074 p.u. PS *d*-axis current and 0.176 p.u. NS *d*-axis current. It can be seen that Scheme 2 can also enhance the small-signal stability of the DFIG system during grid faults. However, according to the theoretical analysis, due to $\Delta\delta_{+} > 0$, Scheme 1 can more effectively suppress the small-signal oscillation of the system than Scheme 2. Fig. 20(b)(iii) shows the DFT analysis results of stator B-phase voltage in Scheme 2. It can be seen that the THD of Scheme 2 is larger than THD of Scheme 1, which is consistent with the theoretical analysis and the correctness of the optimal current control algorithm is further verified.

V. Conclusion

This article investigated the small-signal stability of the DFIG system during asymmetric faults and an improved current control reference algorithm was proposed. The conclusions are summarized as follows.

1) The small-signal state-space model of the grid-connected DFIG system considering the coupling between the PS and NS voltages and currents during the asymmetric faults was established. In addition, the interaction mechanism between the DFIG system and the power grid was explored. It is pointed out that the interaction causes the risk of small-signal instability in the DFIG system during the asymmetrical FRT.
2) The modal analysis based on the mathematical model shows that the unstable poles of the DFIG system are mainly affected by the PLL under asymmetric faults. Combined with the coupling relationships between the PS and NS voltages and currents, the phenomenon that the damping ratio of PLL was influenced by both PS and NS currents was discovered.
3) According to the vector diagram analysis, there are two inherent coupling relationships, which need to be satisfied by controlling the *dq*-axis components of PS and NS currents during the asymmetric faults. When the special coupling relationships, which make the damping ratio of PLL the highest, are satisfied, the system can achieve the optimal small-signal stability. Furthermore, the optimal PS and NS *d*-axis currents reference values satisfying the special coupling relationships are derived.
4) An adaptive optimal current control reference algorithm considering the current capacity limitation of DFIG-based WT was proposed. The detailed simulation and experimental results show the proposed strategy can effectively improve the small-signal stability of the DFIG system during the asymmetrical FRT.

APPENDIX

A. Time-Domain Simulation System Parameters

1) Rated Power: 150 MW; rated voltage: 690 V;
2) DC-link voltage: 1200 V;
3) Turn ratio (*Ns*/*Nr*): 0.4; pole pairs: 2;
4) $R_s = 0.022$ p.u.; $L_s = 2.953$ p.u.;
5) $R_r = 0.026$ p.u.; $L_r = 2.94$ p.u.;
6) $L_m = 2.78$ p.u.;
7) $\mathbf{Z}_G = 0.0162 + j0.0742$ p.u.;
8) $\mathbf{Z}_D = 0.0753 + j0.4262$ p.u.;
9) PLL bandwidth: 23 Hz;
10) PS current closed loop (CCL) bandwidth: 295 Hz;
11) NS CCL bandwidth: 323 Hz;
12) Sampling frequency: 2.5 kHz;
13) Switching frequency: 2.5 kHz;
14) Fault resistance: 0.019 p.u.

B. Experimental System Parameters

1) Rated power: 3 kW; Rated voltage: 220 V;
2) DC-link voltage: 400 V;
3) Turn ratio (*Ns*/*Nr*): 0.517; Pole pairs: 2;
4) $R_s = 0.068$ p.u.; $L_s = 1.285$ p.u.;
5) $R_r = 0.096$ p.u.; $L_r = 1.346$ p.u.;
6) $L_m = 1.258$ p.u.;
7) $R_L = 0.093$ p.u.; $L_L = 0.409$ p.u.;
8) PLL bandwidth: 23 Hz;
9) Synchronous speed: 1500 r/min;
10) Sampling frequency: 10 kHz;
11) Switching frequency: 10 kHz;
12) Fault resistance: 0.099 p.u.

C. Detailed Expressions of Coefficient in (13)

$$\boldsymbol{C}_{A1} = -\frac{\omega_b\left(L_{DT22}R_{G11} - L_{DT12}R_{G21}\right)}{L_{\mathrm{DT21}}L_{\mathrm{DT12}} - L_{\mathrm{DT11}}L_{\mathrm{DT22}}} - j\omega_{\mathrm{pll}+}\frac{\omega_b\left(L_{DT22}L_{G11} - L_{DT12}L_{G21}\right)}{L_{DT21}L_{DT12} - L_{DT11}L_{DT22}}$$

$$C_{B1} = \frac{\omega_b L_{DT22}}{L_{DT21}L_{DT12} - L_{DT11}L_{DT22}}$$

$$C_{C1} = \frac{\omega_b L_{DT12}}{L_{DT21}L_{DT12} - L_{DT11}L_{DT22}}$$

$$\boldsymbol{C}_{\mathrm{D1}} = \frac{\omega_b\left(L_{DT22}R_{DT11} - L_{DT12}R_{DT21}\right)}{L_{DT21}L_{DT12} - L_{DT11}L_{DT22}} - j\omega_{\mathrm{pll}+}\omega_b,$$

$$C_{E1} = \frac{\omega_b\left(L_{DT22}R_{DT12} - L_{DT12}R_{DT22}\right)}{L_{DT21}L_{DT12} - L_{DT11}L_{DT22}}$$

$$\boldsymbol{C}_{A2} = \frac{\omega_b\left(L_{DT21}R_{G11} - L_{DT11}R_{G21}\right)}{L_{DT21}L_{DT12} - L_{DT11}L_{DT22}} - j\omega_{\mathrm{pll}+}\frac{\omega_b\left(L_{DT21}L_{G11} - L_{DT11}L_{G21}\right)}{L_{DT21}L_{DT12} - L_{DT11}L_{DT22}}$$

$$C_{B2} = -\frac{\omega_b L_{DT21}}{L_{DT21}L_{DT12} - L_{DT11}L_{DT22}}$$

$$C_{C2} = \frac{\omega_b L_{DT11}}{L_{DT21}L_{DT12} - L_{DT11}L_{DT22}}$$

$$C_{D2} = -\frac{\omega_b\left(L_{DT21}R_{DT11} - L_{DT11}R_{DT21}\right)}{L_{DT21}L_{DT12} - L_{DT11}L_{DT22}}$$

$$\boldsymbol{C}_{E2} = -\frac{\omega_b\left(L_{DT21}R_{DT12} - L_{DT11}R_{DT22}\right)}{L_{DT21}L_{DT12} - L_{DT11}L_{DT22}} + j\omega_{\mathrm{pll}+}\omega_b.$$

D. Derivation of Small-Signal State-Space Model

The detailed derivation of the small-signal state-space model is given in this section. Linearizing (1)–(7) and (13)–(16)

$$\begin{cases}\Delta\dot{I}^+_{sd+} = -\frac{\omega_b R_s}{\sigma L_s}\Delta I^+_{sd+} + \omega_b(\omega_{\mathrm{pll}0+} + \frac{\omega_r L_m^2}{\sigma L_s L_r})\Delta I^+_{sq+} \\ \quad +\omega_b I^+_{sq0+}\Delta\omega_{\mathrm{pll}+} \\ \quad +\frac{\omega_b L_m R_r}{\sigma L_s L_r}\Delta I^+_{rd+} + \frac{\omega_b L_m\omega_r}{\sigma L_s}\Delta I^+_{rq+} + \frac{\omega_b}{\sigma L_s}\Delta U^+_{sd+} \\ \quad -\frac{\omega_b L_m}{\sigma L_s L_r}\Delta U^+_{rd+} \\ \Delta\dot{I}^+_{sq+} = -\frac{\omega_b R_s}{\sigma L_s}\Delta I^+_{sq+} - \omega_b(\omega_{\mathrm{pll}0+} + \frac{\omega_r L_m^2}{\sigma L_s L_r})\Delta I^+_{sd+} \\ \quad -\omega_b I^+_{sd0+}\Delta\omega_{\mathrm{pll}+} \\ \quad +\frac{\omega_b L_m R_r}{\sigma L_s L_r}\Delta I^+_{rq+} - \frac{\omega_b L_m\omega_r}{\sigma L_s}\Delta I^+_{rd+} + \frac{\omega_b}{\sigma L_s}\Delta U^+_{sq+} \\ \quad -\frac{\omega_b L_m}{\sigma L_s L_r}\Delta U^+_{rq+}\end{cases} \tag{D1}$$

$$\begin{cases}\Delta\dot{I}^-_{sd-} = -\frac{\omega_b R_s}{\sigma L_s}\Delta I^-_{sd-} + \omega_b(-\omega_{\mathrm{pll}0+} + \frac{\omega_r L_m^2}{\sigma L_s L_r})\Delta I^-_{sq-} \\ -\omega_b I^-_{sq0-}\Delta\omega_{\mathrm{pll}+} \\ \quad +\frac{\omega_b L_m R_r}{\sigma L_s L_r}\Delta I^-_{rd-} + \frac{\omega_b L_m\omega_r}{\sigma L_s}\Delta I^-_{rq-} + \frac{\omega_b}{\sigma L_s}\Delta U^-_{sd-} \\ -\frac{\omega_b L_m}{\sigma L_s L_r}\Delta U^-_{rd-} \\ \Delta\dot{I}^-_{sq-} = -\frac{\omega_b R_s}{\sigma L_s}\Delta I^-_{sq-} - \omega_b(-\omega_{\mathrm{pll}0+} + \frac{\omega_r L_m^2}{\sigma L_s L_r})\Delta I^-_{sd-} \\ +\omega_b I^-_{sd0-}\Delta\omega_{\mathrm{pll}+} \\ \quad +\frac{\omega_b L_m R_r}{\sigma L_s L_r}\Delta I^-_{rq-} - \frac{\omega_b L_m\omega_r}{\sigma L_s}\Delta I^-_{rd-} + \frac{\omega_b}{\sigma L_s}\Delta U^-_{sq-} \\ -\frac{\omega_b L_m}{\sigma L_s L_r}\Delta U^-_{rq-}\end{cases} \tag{D2}$$

$$\begin{cases}\Delta\dot{I}^+_{rd+} = \frac{\omega_b L_m R_s}{\sigma L_s L_r}\Delta I^+_{sd+} - \frac{\omega_b L_m\omega_r}{\sigma L_r}\Delta I^+_{sq+} + \omega_b(\omega_{\mathrm{pll}0+} \\ -\frac{\omega_r}{\sigma})\Delta I^+_{rq+} \\ \quad -\frac{\omega_b R_r}{\sigma L_r}\Delta I^+_{rd+} + \omega_b I^+_{rq0+}\Delta\omega_{\mathrm{pll}+} - \frac{\omega_b L_m}{\sigma L_s L_r}\Delta U^+_{sd+} \\ +\frac{\omega_b}{\sigma L_r}\Delta U^+_{rd+} \\ \Delta\dot{I}^+_{rq+} = \frac{\omega_b L_m R_s}{\sigma L_s L_r}\Delta I^+_{sq+} + \frac{\omega_b L_m\omega_r}{\sigma L_r}\Delta I^+_{sd+} - \omega_b(\omega_{\mathrm{pll}0+} \\ -\frac{\omega_r}{\sigma})\Delta I^+_{rd+} \\ \quad -\frac{\omega_b R_r}{\sigma L_r}\Delta I^+_{rq+} - \omega_b I^+_{rd0+}\Delta\omega_{\mathrm{pll}+} - \frac{\omega_b L_m}{\sigma L_s L_r}\Delta U^+_{sq+} \\ +\frac{\omega_b}{\sigma L_r}\Delta U^+_{rq+}\end{cases} \tag{D3}$$

$$\begin{cases}\Delta\dot{I}^-_{rd-} = \frac{\omega_b L_m R_s}{\sigma L_s L_r}\Delta I^-_{sd-} - \frac{\omega_b L_m\omega_r}{\sigma L_r}\Delta I^-_{sq-} - \omega_b(\omega_{\mathrm{pll}0+} \\ +\frac{\omega_r}{\sigma})\Delta I^-_{rq-} \\ \quad -\frac{\omega_b R_r}{\sigma L_r}\Delta I^-_{rd-} - \omega_b I^-_{rq0-}\Delta\omega_{\mathrm{pll}+} - \frac{\omega_b L_m}{\sigma L_s L_r}\Delta U^-_{sd-} \\ +\frac{\omega_b}{\sigma L_r}\Delta U^-_{rd-} \\ \Delta\dot{I}^-_{rq-} = \frac{\omega_b L_m R_s}{\sigma L_s L_r}\Delta I^-_{sq-} + \frac{\omega_b L_m\omega_r}{\sigma L_r}\Delta I^-_{sd-} + \omega_b(\omega_{\mathrm{pll}0+} \\ +\frac{\omega_r}{\sigma})\Delta I^-_{rd-} \\ \quad -\frac{\omega_b R_r}{\sigma L_r}\Delta I^-_{rq-} + \omega_b I^-_{rd0-}\Delta\omega_{\mathrm{pll}+} - \frac{\omega_b L_m}{\sigma L_s L_r}\Delta U^-_{sq-} \\ +\frac{\omega_b}{\sigma L_r}\Delta U^-_{rq-}\end{cases} \tag{D4}$$

$$\begin{cases}\Delta\dot{x}_{1\pm}=-\Delta I^{\pm}_{rd\pm},\Delta\dot{x}_{2\pm}=-\Delta I^{\pm}_{rq\pm}\\ \Delta\dot{x}_{3+}=\Delta I^{*+}_{gd+}-\Delta I^{+}_{gd+},\Delta\dot{x}_{3-}=-\Delta I^{-}_{gd-}\\ \Delta\dot{x}_{4\pm}=-\Delta I^{\pm}_{gq\pm}\end{cases}\tag{D5}$$

$$\begin{cases}\Delta\dot{I}^{+}_{Dd+}=R_{A1}U^{+}_{Gq0+}\Delta\theta_{\text{pll}+}+C_{B1}\Delta U^{+}_{sd+}+C_{C1}\Delta U^{-}_{sd-}\\ +R_{D1}\Delta I^{+}_{Dd+}\\ +C_{E1}\Delta I^{-}_{Dd-}+\omega_{\text{pll}0+}\left(L_{A1}U^{+}_{Gd0+}\Delta\theta_{\text{pll}+}-L_{D1}\Delta I^{+}_{Dq+}\right)\\ +\left(-L_{A1}U^{+}_{Gq0+}-L_{D1}I^{+}_{Dq0+}\right)\Delta\omega_{\text{pll}+}\\ \Delta\dot{I}^{+}_{Dq+}=-R_{A1}U^{+}_{Gd0+}\Delta\theta_{\text{pll}+}+\mathrm{C}_{B1}\Delta U^{+}_{sq+}-C_{C1}\Delta U^{-}_{sq-}\\ +R_{D1}\Delta I^{+}_{Dq+}\\ -C_{E1}I^{-}_{Dq-}+\omega_{\text{pll}0+}\left(L_{A1}U^{+}_{Gq0+}\Delta\theta_{\text{pll}+}+L_{D1}\Delta I^{+}_{Dd+}\right)\\ +\left(L_{A1}U^{+}_{Gd0+}+L_{D1}I^{+}_{Dd0+}\right)\Delta\omega_{\text{pll}+}\end{cases}\tag{D6}$$

$$\begin{cases}\Delta\dot{I}^{-}_{Dd-}=R_{A2}U^{+}_{Gq0+}\Delta\theta_{\text{pll}+}+C_{B2}\Delta U^{+}_{sd+}\\ +C_{C2}\Delta U^{-}_{sd-}+C_{D2}\Delta I^{+}_{Dd+}\\ +R_{E2}\Delta I^{-}_{Dd-}+\omega_{\text{pll}0+}\left(L_{A2}U^{+}_{Gd0+}\Delta\theta_{\text{pll}+}+L_{E2}\Delta I^{-}_{Dq-}\right)\\ +\left(-L_{A2}U^{+}_{Gq0+}+L_{E2}I^{-}_{Dq0-}\right)\Delta\omega_{\text{pll}+}\\ \Delta\dot{I}^{-}_{Dq-}=R_{A2}U^{+}_{Gd0+}\Delta\theta_{\text{pll}+}-C_{B2}\Delta U^{+}_{sq+}+C_{C2}\Delta U^{-}_{sq-}\\ -C_{D2}\Delta I^{+}_{Dq+}\\ +R_{E2}I^{-}_{Dq-}-\omega_{\text{pll}0+}\left(L_{A2}U^{+}_{Gq0+}\Delta\theta_{\text{pll}+}+L_{E2}\Delta I^{-}_{Dd-}\right)\\ -\left(L_{A2}U^{+}_{Gd0+}+L_{E2}I^{-}_{Dd0-}\right)\Delta\omega_{\text{pll}+}\end{cases}\tag{D7}$$

$$\begin{cases}\Delta\dot{U}^{+}_{sd+}=\frac{\omega_b}{C_f}\left(\Delta I^{+}_{Dd+}-\Delta I^{+}_{sd+}-\Delta I^{+}_{gd+}\right)\\ +\omega_{\text{pll}0+}\omega_b\Delta U^{+}_{sq+}+\omega_b U^{+}_{sq0+}\Delta\omega_{\text{pll}+}\\ \Delta\dot{U}^{+}_{sq+}=\frac{\omega_b}{C_f}\left(\Delta I^{+}_{Dq+}-\Delta I^{+}_{sq+}-\Delta I^{+}_{gq+}\right)\\ -\omega_{\text{pll}0+}\omega_b\Delta U^{+}_{sd+}-\omega_b U^{+}_{sd0+}\Delta\omega_{\text{pll}+}\\ \Delta\dot{U}^{-}_{sd-}=\frac{\omega_b}{C_f}\left(\Delta I^{-}_{Dd-}-\Delta I^{-}_{sd-}-\Delta I^{-}_{gd-}\right)\\ -\omega_{\text{pll}0+}\omega_b\Delta U^{-}_{sq-}-\omega_b U^{-}_{sq0-}\Delta\omega_{\text{pll}+}\\ \Delta\dot{U}^{-}_{sq-}=\frac{\omega_b}{C_f}\left(\Delta I^{-}_{Dq-}-\Delta I^{-}_{sq-}-\Delta I^{-}_{gq-}\right)\\ +\omega_{\text{pll}0+}\omega_b\Delta U^{-}_{sd-}+\omega_b U^{-}_{sd0-}\Delta\omega_{\text{pll}+}\end{cases}\tag{D8}$$

$$\begin{cases}\Delta\dot{I}^{+}_{gd+}=-\frac{\omega_b R_g}{L_g}\Delta I^{+}_{gd+}+\omega_{\text{pll}0+}\omega_b\Delta I^{+}_{gq+}\\ +\omega_b I^{+}_{gq0+}\Delta\omega_{\text{pll}+}-\frac{\omega_b}{L_g}\Delta V^{+}_{gd+}+\frac{\omega_b}{L_g}\Delta U^{+}_{sd+}\\ \Delta\dot{I}^{+}_{gq+}=-\frac{\omega_b R_g}{L_g}\Delta I^{+}_{gq+}-\omega_{\text{pll}0+}\omega_b\Delta I^{+}_{gd+}\\ -\omega_b I^{+}_{gd0+}\Delta\omega_{\text{pll}+}-\frac{\omega_b}{L_g}\Delta V^{+}_{gq+}+\frac{\omega_b}{L_g}\Delta U^{+}_{sq+}\end{cases}\tag{D9}$$

$$\begin{cases}\Delta\dot{I}^{-}_{gd-}=-\frac{\omega_b R_g}{L_g}\Delta I^{-}_{gd-}-\omega_{\text{pll}0+}\omega_b\Delta I^{-}_{gq-}\\ -\omega_b I^{-}_{gq0-}\Delta\omega_{\text{pll}+}-\frac{\omega_b}{L_g}\Delta V^{-}_{gd-}+\frac{\omega_b}{L_g}\Delta U^{-}_{sd-}\\ \Delta\dot{I}^{-}_{gq-}=-\frac{\omega_b R_g}{L_g}\Delta I^{-}_{gq-}+\omega_{\text{pll}0+}\omega_b\Delta I^{-}_{gd-}\\ +\omega_b I^{-}_{gd0-}\Delta\omega_{\text{pll}+}-\frac{\omega_b}{L_g}\Delta V^{-}_{gq-}+\frac{\omega_b}{L_g}\Delta U^{-}_{sq-}\end{cases}\tag{D10}$$

$$\begin{cases}\Delta U^{+}_{rd+}=(R_r-k_{p1+})\Delta I^{+}_{rd+}+k_{i1+}\Delta x_{1+}\\ -\sigma L_r I^{+}_{rq0+}\Delta\omega_{\text{pll}+}\\ -(\omega_{\text{pll}0+}-\omega_r)\sigma L_r\Delta I^{+}_{rq+}+\frac{L_m}{L_s}(\Delta U^{+}_{sd+}\\ -R_s\Delta I^{+}_{sd+}+\omega_r L_s\Delta I^{+}_{sq+})\\ \Delta U^{+}_{rq+}=(R_r-k_{p2+})\Delta I^{+}_{rq+}+k_{i2+}\Delta x_{2+}\\ +\sigma L_r I^{+}_{rd0+}\Delta\omega_{\text{pll}+}\\ +(\omega_{\text{pll}0+}-\omega_r)\sigma L_r\Delta I^{+}_{rd+}\\ +\frac{L_m}{L_s}(\Delta U^{+}_{sq+}-R_s\Delta I^{+}_{sq+}-\omega_r L_s\Delta I^{+}_{sd+})\end{cases}\tag{D11}$$

$$\begin{cases}\Delta U^{-}_{rd-}=(R_r-k_{p1-})\Delta I^{-}_{rd-}+k_{i1-}\Delta x_{1-}\\ +\sigma L_r I^{-}_{rq0-}\Delta\omega_{\text{pll}+}\\ +(\omega_{\text{pll}0+}+\omega_r)\sigma L_r\Delta I^{-}_{rq-}+\frac{L_m}{L_s}(\Delta U^{-}_{sd-}-R_s\Delta I^{-}_{sd-}\\ +\omega_r L_s\Delta I^{-}_{sq-})\\ \Delta U^{-}_{rq-}=(R_r-k_{p2-})\Delta I^{-}_{rq-}+k_{i2-}\Delta x_{2-}\\ -\sigma L_r I^{-}_{rd0-}\Delta\omega_{\text{pll}+}\\ -(\omega_{\text{pll}0+}+\omega_r)\sigma L_r\Delta I^{-}_{rd-}+\frac{L_m}{L_s}(\Delta U^{-}_{sq-}-R_s\Delta I^{-}_{sq-}\\ -\omega_r L_s\Delta I^{-}_{sd-})\end{cases}\tag{D12}$$

$$\begin{cases}\Delta V^{+}_{gd+}=(k_{p3+}-R_g)\Delta I^{+}_{gd+}-k_{i3+}\Delta x_{3+}\\ +\omega_{\text{pll}0+}L_g\Delta I^{+}_{gq+}\\ +L_g I^{+}_{gq0+}\Delta\omega_{\text{pll}+}+\Delta U^{+}_{sd+}\\ \Delta V^{+}_{gq+}=(k_{p4+}-R_g)\Delta I^{+}_{gq+}-k_{i4+}\Delta x_{4+}\\ -\omega_{\text{pll}0+}L_g\Delta I^{+}_{gd+}\\ -L_g I^{+}_{gd0+}\Delta\omega_{\text{pll}+}+\Delta U^{+}_{sq+}\end{cases}\tag{D13}$$

$$\begin{cases}\Delta V^{-}_{gd-}=(k_{p3-}-R_g)\Delta I^{-}_{gd-}-k_{i3-}\Delta x_{3-}\\ -\omega_{\text{pll}0+}L_g\Delta I^{-}_{gq-}-L_g I^{-}_{gq0-}\Delta\omega_{\text{pll}+}+\Delta U^{-}_{sd-}\\ \Delta V^{-}_{gq-}=(k_{p4-}-R_g)\Delta I^{-}_{gq-}-k_{i4-}\Delta x_{4-}\\ +\omega_{\text{pll}0+}L_g\Delta I^{-}_{gd-}+L_g I^{-}_{gd0-}\Delta\omega_{\text{pll}+}+\Delta U^{-}_{sq-}\end{cases}\tag{D14}$$

$$\begin{cases}\Delta\dot{x}_5=-\Delta U^{+}_{\text{dc}+}\\ \Delta I^{*+}_{gd+}=k_{p5+}\Delta\dot{x}_5+k_{i5+}\Delta x_5\\ \Delta\dot{U}^{+}_{\text{dc}+}=\frac{1}{CU^{+}_{\text{dc}0+}}(\Delta U^{+}_{sd+}I^{+}_{gd0+}+U^{+}_{sd0+}\Delta I^{+}_{gd+}\\ +\Delta U^{+}_{sq+}I^{+}_{gq0+}+U^{+}_{sq0+}\Delta I^{+}_{gq+}\\ +\Delta U^{-}_{sd-}I^{-}_{gd0-}+U^{-}_{sd0-}\Delta I^{-}_{gd-}\\ +\Delta U^{-}_{sq-}I^{-}_{gq0-}+U^{-}_{sq0-}\Delta I^{-}_{gq-})\\ -\frac{1}{CU^{+}_{\text{dc}0+}}(\Delta U^{+}_{rd+}I^{+}_{rd0+}+U^{+}_{rd0+}\Delta I^{+}_{rd+}\\ +\Delta U^{+}_{rq+}I^{+}_{rq0+}+U^{+}_{rq0+}\Delta I^{+}_{rq+}\\ +\Delta U^{-}_{rd-}I^{-}_{rd0-}+U^{-}_{rd0-}\Delta I^{-}_{rd-}\\ +\Delta U^{-}_{rq-}I^{-}_{rq0-}+U^{-}_{rq0-}\Delta I^{-}_{rq-})\end{cases}\tag{D15}$$

$$\begin{cases}\Delta\dot{\theta}_{\text{pll}+}=\omega_b\Delta\omega_{\text{pll}+}\\ \Delta\dot{x}_6=\Delta U^{+}_{sq+}\\ \Delta\omega_{\text{pll}+}=k_{p6+}\Delta U^{+}_{sq+}+k_{i6+}\Delta x_6.\end{cases}\tag{D16}$$

Based on (D1)–(D16), the linearized state-space equation of the DFIG system can be obtained as

$$\begin{cases}\Delta\dot{\boldsymbol{x}}=\boldsymbol{A}\Delta\boldsymbol{x}+\boldsymbol{B}\Delta\boldsymbol{u}\\ 0=\boldsymbol{C}\Delta\boldsymbol{x}+\boldsymbol{D}\Delta\boldsymbol{u}.\end{cases}\tag{D17}$$

REFERENCES

[1] R. Cardenas, R. Pena, S. Alepuz, and G. Asher, "Overview of control systems for the operation of DFIGs in wind energy applications," *IEEE Trans. Ind. Electron.*, vol. 60, no. 7, pp. 2776–2798, Jul. 2013.

[2] F. Blaabjerg, M. Liserre, and K. Ma, "Power electronics converters for wind turbine systems," *IEEE Trans. Ind. Appl.*, vol. 48, no. 2, pp. 708–719, Mar./Apr. 2012.

[3] L. Fan and Z. Miao, "An explanation of oscillations due to wind power plants weak grid interconnection," *IEEE Trans. Sustain. Energy*, vol. 9, no. 1, pp. 488–490, Jan. 2018.

[4] X. Zhang, D. Xia, Z. Fu, G. Wang, and D. Xu, "An improved feedforward control method considering PLL dynamics to improve weak grid stability of grid-connected inverters," *IEEE Trans. Ind. Appl.*, vol. 54, no. 5, pp. 5143–5151, Sep./Oct. 2018.

[5] X. Wang, J. Yao, J. Pei, P. Sun, H. Zhang, and R. Liu, "Analysis and damping control of small-signal oscillations for VSC connected to weak AC grid during LVRT," *IEEE Trans. Energy Convers.*, vol. 34, no. 3, pp. 1667–1676, Sep. 2019.

[6] J. Hu, B. Wang, W. Wang, H. Tang, Y. Chi, and Q. Hu, "Small signal dynamics of DFIG-based wind turbines during riding through symmetrical faults in weak AC grid," *IEEE Trans. Energy Convers.*, vol. 32, no. 2, pp. 720–730, Jun. 2017.

[7] J. Kim, E. Muljadi, J.-W. Park, and Y. C. Kang, "Adaptive hierarchical voltage control of a DFIG-based wind power plant for a grid fault," *IEEE Trans. Smart Grid*, vol. 7, no. 6, pp. 2980–2990, Nov. 2016.

[8] X. Tian, H. Tang, Y. Li, Y. Chi, and Y. Su, "Dynamic stability of weak grid connection of large-scale DFIG based on wind turbines," *J. Eng.*, vol. 2017, no. 13, pp. 1092–1097, 2017.

[9] D. Shin, K.-J. Lee, J.-P. Lee, D.-W. Yoo, and H.-J. Kim, "Implementation of fault ride-through techniques of grid-connected inverter for distributed energy resources with adaptive low-pass notch PLL," *IEEE Trans. Power Electron.*, vol. 30, no. 5, pp. 2859–2871, May 2015.

[10] C. Ye, J. Ying, J. Hu, Y. Wang, and N. Wang, "Rotor dynamics of DFIG wind turbines under grid faults," in *Proc. Int. Conf. Renewable Power Gener.*, 2015, pp. 1–5.

[11] R. Liu, J. Yao, X. Wang, P. Sun, J. Pei, and J. Hu, "Dynamic stability analysis and improved LVRT schemes of DFIG-based wind turbines during a symmetrical fault in a weak grid," *IEEE Trans. Power Electron.*, vol. 35, no. 1, pp. 303–318, Jan. 2020.

[12] L. Huang *et al.*, "Grid-synchronization stability analysis and loop shaping for PLL-based power converters with different reactive power control," *IEEE Trans. Smart Grid*, vol. 11, no. 1, pp. 501–516, Jan 2020.

[13] L. Chen, B. Zhang, and X. Fan, "Asymmetrical fault ride-through control strategy for rotor-side converter of DFIG," *IEEE Trans. Energy Convers.*, vol. 35, no. 2, pp. 1046–1053, Jun. 2020.

[14] Y. M. Alsmadi *et al.*, "Detailed investigation and performance improvement of the dynamic behavior of grid-connected DFIG-based wind turbines under LVRT conditions," *IEEE Trans. Ind. Appl.*, vol. 54, no. 5, pp. 4795–4812, Sep./Oct. 2018.

[15] T. Neumann, T. Wijnhoven, G. Deconinck, and I. Erlich, "Enhanced dynamic voltage control of type 4 wind turbines during unbalanced grid faults," *IEEE Trans. Energy Convers.*, vol. 30, no. 4, pp. 1650–1659, Dec. 2015.

[16] Technical *Requirements for the Connection and Operation of Customer Installations to the High-Voltage Network* (TCC *High Voltage*), Standard VDE-AR-N 4120, 2015.

[17] J. Hu, H. Xu, and Y. He, "Coordinated control of DFIG's RSC and GSC under generalized unbalanced and distorted grid voltage conditions," *IEEE Trans. Ind. Electron.*, vol. 60, no. 7, pp. 2808–2819, Jul. 2013.

[18] K. Ma, M. Liserre, and F. Blaabjerg, "Power controllability of three-phase converter with unbalanced AC source," in *Proc. 28th Annu. IEEE Appl. Power Electron. Conf. Expo.*, Long Beach, CA, USA, 2013, pp. 342–350.

[19] R. Liu, J. Yao, P. Sun, J. Pei, H. Zhang, and Y. Zhao, "Complex impedance-based frequency coupling characteristics analysis of DFIG-based WT during asymmetric grid faults," *IEEE Trans. Ind. Electron.*, to be published.

[20] H.-S. Song and K. Nam, "Dual current control scheme for PWM converter under unbalanced input voltage conditions," *IEEE Trans. Ind. Electron.*, vol. 46, no. 5, pp. 953–959, Oct. 1999.

[21] H. Wang, W. Zhang, J. Hu, and Y. He, "Improved dual-PI rotor current control scheme for a wind-driven DFIG during asymmetrical grid voltage dips," in *Proc. IEEE Int. Electr. Mach. Drives Conf.*, Miami, FL, USA, 2009, pp. 171–176.

[22] H. Yuan, H. Xin, L. Huang, Z. Wang, and D. Wu, "Stability analysis and enhancement of type-4 wind turbines connected to very weak grids under severe voltage sags," *IEEE Trans. Energy Convers.*, vol. 34, no. 2, pp. 838–848, Jun. 2019.

[23] T. Wang, H. Nian, Z. Q. Zhu, H. Huang, and X. Huang, "Flexible PCC voltage unbalance compensation strategy for autonomous operation of parallel DFIGs," *IEEE Trans. Ind. Appl.*, vol. 53, no. 5, pp. 4807–4820, Sep./Oct. 2017.

[24] E. Nasr-Azadani, C. A. Canizares, D. E. Olivares, and K. Bhattacharya, "Stability analysis of unbalanced distribution systems with synchronous machine and DFIG based distributed generators," *IEEE Trans. Smart Grid*, vol. 5, no. 5, pp. 2326–2338, Sep. 2014.

[25] D. Sun and X. Wang, "Low-complexity model predictive direct power control for DFIG under both balanced and unbalanced grid conditions," *IEEE Trans. Ind. Electron.*, vol. 63, no. 8, pp. 5186–5196, Aug. 2016.

[26] B. Wang, S. Wang, and J. Hu, "Dynamic modeling of asymmetrical-faulted grid by decomposing coupled sequences via complex vector," *IEEE J. Emerg. Sel. Topics Power Electron.*, to be published.

[27] S. Kurokawa, R. S. Daltin, A. J. Prado, and J. Pissolato, "An alternative modal representation of a symmetrical nontransposed three-phase transmission line," *IEEE Trans. Power Syst.*, vol. 22, no. 1, pp. 500–501, Feb. 2007.

[28] L. Harnefors, "Modeling of three-phase dynamic systems using complex transfer functions and transfer matrices," *IEEE Trans. Ind. Electron.*, vol. 54, no. 4, pp. 2239–2248, Aug. 2007.

[29] X. Zeng, J. Yao, Z. Chen, W. Hu, Z. Chen, and T. Zhou, "Co-ordinated control strategy for hybrid wind farms with PMSG and FSIG under unbalanced grid voltage condition," *IEEE Trans. Sustain. Energy*, vol. 7, no. 3, pp. 1100–1110, Jul. 2016.

[30] H. Yuan, X. Yuan, and J. Hu, "Modeling and large-signal stability of DFIG wind turbine in dc-voltage control time scale," in *Proc. IEEE Power Energy Soc. Gen. Meeting*, Boston, MA, USA, 2016, pp. 1–5.

[31] J. Pei *et al.*, "Characteristic analysis and risk assessment for voltage–frequency coupled transient instability of large-scale grid-connected renewable energy plants during LVRT," *IEEE Trans. Ind. Electron.*, vol. 67, no. 7, pp. 5515–5530, Jul. 2020.

[32] D. P. Bertsekas, *Constrained Optimization and Lagrange Multiplier Methods*. New York, NY, USA, Academic, 1982.

[33] B. Wang, J. Suonan, H. Liu, and G. Song, "Long transmission lines fault location based on parameter identification using one-terminal data," in *Proc. Asia-Pacific Power Energy Eng. Conf.*, 2012, pp. 1–4.

[34] L. M. Fernández, C. A. García, J. R. Saenz, and F. Jurado, "Equivalent models of wind farms by using aggregated wind turbines and equivalent winds," *Energy Convers. Manage.*, vol. 50, no. 3, pp. 691–704, Mar. 2009.

Xin Fang received the B.Eng. degree in electrical engineering and automation from the Shenyang University of Technology, Shenyang, China, in 2019. She is currently working toward the M.Sc. degree with the School of Electrical Engineering, Chongqing University, Chongqing, China.

Her research interests include electric machines control and the control of wind turbine generation system.

Jun Yao (Member, IEEE) received the B.Eng., M.Sc., and Ph.D. degrees from Chongqing University, Chongqing, China, in 2001, 2004, and 2007, respectively, all in electrical engineering.

Since 2004, he has been with the School of Electrical Engineering, Chongqing University, Chongqing, where he is currently a Professor. From 2012 to 2013, he was a Visiting Researcher with the Department of Energy Technology, Aalborg University, Aalborg, Denmark. He is the author/co-author of more than 100 peer-reviewed technical papers and holds more than 20 issued/pending patents. His research interests include electric machines control, power electronics conversion and control, renewable power generation, and mainly wind energy and power electronics application to the power systems.

Dr. Yao is a member of IEC SC8A JWG5.

Ruikuo Liu received the B.Eng. and M.Sc. degrees from Southwest Jiaotong University, Chengdu, China, in 2009 and 2012, respectively, both in electrical engineering, and the Ph.D. degree from the School of Electrical Engineering, Chongqing University, Chongqing, China, in 2020.

His research interests include electric machines control, control of wind turbine generation system, and renewable power generation.

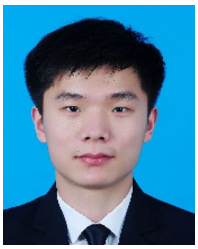

Yang Zhao received the B.Eng. degree in ship electronic and electrical engineering from Dalian Maritime University, Dalian, China, in 2018. He is currently working toward the M.S. degree with the School of Electrical Engineering, Chongqing University, Chongqing, China.

His research interests include electric machines control, modeling and control of wind turbine generation system, and renewable power generation.

Peng Sun received the B.Eng. degree in electrical engineering and automation from Anhui University, Hefei, China, in 2017. He is currently working toward the Ph.D. degree with the School of Electrical Engineering, Chongqing University, Chongqing, China.

His research interests include electric machines control, modeling and control of wind turbine generation system, and renewable power generation.

Sen Huang received the B.Eng. degree in electrical engineering and automation from Northwest A&F University, Xianyang, China, in 2019. He is currently working toward the Ph.D. degree with the School of Electrical Engineering, Chongqing University, Chongqing, China.

His research interests include electric machines control, modeling and control of wind turbine generation system, and renewable power generation.